Small-scale shear layers in isotropic turbulence of viscoelastic fluids

Tomoaki Watanabe,[1]† Hugo Abreu,[2] Koji Nagata,[1] and Carlos B. da Silva[2]

[1]Department of Mechanical Engineering and Science, Kyoto University, Kyoto, Japan

[2]LAETA, IDMEC, Instituto Superior Técnico, Universidade de Lisboa, Lisboa, Portugal

(Received xx; revised xx; accepted xx)

Small-scale shear layers arising from the turbulent motion of viscoelastic fluids are investigated through direct numerical simulations of statistically steady, homogeneous isotropic turbulence in a fluid described by the FENE-P model. These shear layers are identified via a triple decomposition of the velocity gradient tensor. The viscoelastic effects are examined through the Weissenberg number (Wi), representing the ratio of the longest polymer relaxation time scale to the Kolmogorov time scale. The mean flow around these shear layers is analysed within a local reference frame that characterises shear orientation. In both Newtonian and viscoelastic turbulence, shear layers appear in a straining flow, featuring stretching in the shear-vorticity direction and compression in the layer-normal direction. Polymer stresses are markedly influenced by the shear and strain, which enhance kinetic energy dissipation due to the polymers. The shear layers in viscoelastic turbulence exhibit a high aspect ratio, undergoing significant characteristic changes once Wi exceeds approximately 2. As Wi increases, the extensive strain weakens, diminishing vortex stretching. This change coincides with an imbalance between extension and compression in the straining flow. In the shear layer, the interaction between vorticity and polymer stress causes the destruction and production of enstrophy at low and high Wi values, respectively. Enstrophy production at high Wi is induced by normal polymer stress oriented along the shear flow, associated with the diminished extensive strain. The Wi-dependent behaviour of these shear layers aligns with the overall flow characteristics, underscoring their pivotal roles in vorticity dynamics and kinetic energy dissipation in viscoelastic turbulence.

1. Introduction

The addition of a very small fraction of macromolecules into a Newtonian solvent (typically water) can lead to massive drag reductions of up to 80% (Toms 1948). This has led to much practical research due to its potential engineering applications, and many studies have focused on understanding the physical mechanisms associated with the drag reduction. Although the majority of the investigations have focused on wall-bounded flows (e.g. Li & Graham 2007; White & Mungal 2008; Graham 2014), many recent investigations have focused on homogenous isotropic turbulence (HIT) in order to focus on the details of the energy cascade mechanism in these flows (De Angelis *et al.* 2005; Ouellette *et al.* 2009). In particular, detailed investigations have been devoted to the kinetic energy flux within the

† Email address for correspondence: watanabe.tomoaki.8x@kyoto-u.ac.jp

modified energy cascade mechanism and the shape of the kinetic energy spectrum in turbulent flows of viscoelastic fluids (Valente *et al.* 2014*a*, 2016). The classical (non-linear) energy cascade flux decreases in inertial-elastic turbulence, with a concomitant increase of the kinetic energy directly dissipated by the polymers. At high Weissenberg numbers, which are defined as the ratio between the maximum polymer relaxation time scale and the Kolmogorov time scale, the polymers initiate a polymer-induced energy cascade from large to small scales. This process alters the mechanisms of energy transfer and is accompanied by modifications in the shape of the energy spectra. Equivalent modifications can also be examined in real space using velocity structure functions. Alterations in the spectra and structure functions due to polymers have been observed in direct numerical simulations (DNS) of isotropic turbulence (Valente *et al.* 2014*a*, 2016) and in experiments on turbulence generated by a grid (Vonlanthen & Monkewitz 2013) or by counter-rotating baffled discs (Ouellette *et al.* 2009). The detailed definition of the Weissenberg number Wi is given in § 2. The same definition of Wi is consistently used throughout the paper. The modification of the energy cascade caused by the polymers results in a reduced solvent dissipation rate compared to Newtonian turbulence, since part of the classical energy flux within the solvent eventually finds its way into the polymer molecules, where the kinetic energy is stored. Since the drag in a pipe or a channel can be related to the dissipation rate within the fluid, this dissipation reduction observed for isotropic turbulence can be seen as a drag reduction, as described in previous studies (Kalelkar *et al.* 2005; Perlekar *et al.* 2006; Cai *et al.* 2010; Ferreira *et al.* 2016).

The small-scale turbulent structures are important in understanding the energy dissipation process in turbulence (Tsinober 2009). The structures are also explored for understanding complex turbulent flows in terms of simplified structural models (Adrian *et al.* 2000). Small-scale turbulent motions are often studied by analysing the velocity gradient tensor $\nabla \boldsymbol{u}$. Throughout the paper, subscript indices are used to specify components of tensors and vectors. The velocity gradient tensor is often analysed with decompositions by which particular types of local fluid motion are extracted. In a classical double decomposition, it is split into symmetric and antisymmetric components as $(\nabla \boldsymbol{u})_{ij} = S_{ij} + \Omega_{ij}$ with the rate-of-strain tensor $S_{ij} = (\partial u_i/\partial x_j + \partial u_j/\partial x_i)/2$ and the rate-of-rotation tensor $\Omega_{ij} = (\partial u_i/\partial x_j - \partial u_j/\partial x_i)/2$. Turbulence is characterised by vortices with rotating motion, which contributes to Ω_{ij} (Corrsin & Kistler 1955). Small-scale vortices, in particular, have received significant attention in turbulence research. Early investigations of vortices used enstrophy $\omega^2/2 = \Omega_{ij}\Omega_{ij}$ for vortex identification. Here, successive indices imply summation. Flow regions with large enstrophy frequently exhibit a tubular shape (Jiménez *et al.* 1993). These small-scale tubular vortices are called vortex tubes, worms or vortex filaments and have been extensively studied in previous studies, where the scalings of the diameter, azimuthal velocity, stretching rate and other properties have been revealed for various turbulent flows (Siggia 1981; Vincent & Meneguzzi 1991; Jiménez & Wray 1998; Tanahashi *et al.* 2001; Kang & Meneveau 2008; Ganapathisubramani *et al.* 2008; da Silva *et al.* 2011; Jahanbakhshi *et al.* 2015; Watanabe *et al.* 2017; Ghira *et al.* 2022).

The vortical structures in turbulent flows of viscoelastic fluids have been analysed in several works. The drag reduction observed in wall-bounded flows is associated with the weakening and suppressing of the streamwise vortices (Li & Graham 2007; Kim *et al.* 2007). Guimarães *et al.* (2020, 2022) reported that the large-scale eddies in turbulent jets and wakes of viscoelastic fluids are substantially different from the ones observed in Newtonian free shear flows: they appear to be more elongated and showing more sheet-like shapes as the Weissenberg number increases. It is noteworthy that the large-scale eddies obtained in the simulations by Guimarães *et al.* (2020, 2022) closely resemble the experimental visualisations

reported in Yamani *et al.* (2023). Compared to turbulent free flows of Newtonian fluids, a significant decrease of the entrainment rate observed in these flows is caused by the depletion of small-scale structures due to the viscoelasticity (Abreu *et al.* 2022). Vortical structures in HIT of viscoelastic fluids have been extensively analysed, as noted in various studies including Perlekar *et al.* (2006) and Cai *et al.* (2010). It has been observed that intense vorticity structures in DNS of HIT in viscoelastic fluids typically manifest as sheets rather than tubes. However, the characteristics of these structures have yet to be investigated in much detail, except in Horiuti *et al.* (2013), where the observed drag reduction reported for viscoelastic fluids is explained in relation to the dynamics of these structures. In high drag-reduction cases, the creation of vortex tubes due to the roll-up of sheets is hindered by tensile forces.

When vortical structures in Newtonian fluids are identified from an enstrophy field, sheet-like structures are also observed together with the vortex tubes (Vincent & Meneguzzi 1991; Jiménez *et al.* 1993). These structures are known as vortex sheets. In recent studies, they have been simply named shear layers because of intense shear in the layer structures (Eisma *et al.* 2015; Watanabe *et al.* 2020). The present study also names these structures as shear layers because they are identified with a quantity characterising shearing motion. Since Ω_{ij} and S_{ij} are significant for local fluid motion within the shear layers, both vortex tubes and shear layers have been observed in enstrophy visualisation. Various identification methods to detect vortex tubes have been proposed in previous studies. Several identification schemes for vortex tubes rely on the three-dimensional or two-dimensional distribution of quantities associated with these structures, such as the second invariant of the velocity gradient tensor (Chong *et al.* 1990; Jeong & Hussain 1995). Recent advances in this topic have successfully identified vortex tubes as vortical Lagrangian coherent structures (LCSs), as demonstrated by Neamtu-Halic *et al.* (2019), based on the Lagrangian-averaged vorticity deviation (Haller *et al.* 2016). The LCS approach in the detection of turbulent structures has the advantage of defining the boundary of each structure (Green *et al.* 2007; Haller 2023). Once a vortex tube is identified, it is easy to determine two characteristic orientations of the structure, namely a vortex axis and radial direction. Thus, vortex tubes are often studied with a radial profile of flow variables (Jiménez *et al.* 1993; Jahanbakhshi *et al.* 2015), which has helped the investigation of these structures. On the other hand, most studies of shear layers have relied on flow visualisations (Horiuti & Fujisawa 2008; Buxton & Ganapathisubramani 2010; Bhatt & Tsuji 2021). This is likely due to the fact that the common identification method for shear layers uses a scalar quantity to determine the location of these layers (Horiuti & Takagi 2005), but fails to determine their orientation, which is essential in the analysis of these structures.

New identification schemes for vortex tubes have been proposed because of the difficulty in distinguishing vortex tubes and shear layers in the enstrophy field. This difficulty arises from a shear contribution to Ω_{ij}. A parallel shear flow has large Ω_{ij} and S_{ij}, although there is no rotating motion typical of vortex tubes. Therefore, recent vortex identification schemes rely on new decompositions of $\nabla \boldsymbol{u}$. To prevent local shearing motion from blurring a quantity used to identify vortex tubes, the new decompositions often extract a shear component from $\nabla \boldsymbol{u}$. Examples are the triple decomposition (Kolář 2007) and Rortex-based decomposition (Liu *et al.* 2018). These two decompositions are related, although the decomposition algorithms are different. In addition, the triple decomposition can be expressed with a real Schur form, which provides an efficient decomposition algorithm (Kronborg & Hoffman 2023). The mathematical properties of these decompositions have been extensively studied in previous studies, including Galilean invariance (Wang *et al.* 2018). They are also thoroughly studied as the theory of the Schur decomposition (Keylock 2018 and references therein). These decompositions can define an alternative vorticity vector representing rigid-body rotation

by removing the shear contribution (Šístek *et al.* 2012; Maciel *et al.* 2012; Kolář & Šístek 2014).

The shear component of $\nabla \boldsymbol{u}$ in these new decomposition schemes is shown to be helpful in identifying the shear layers in turbulent flows (Eisma *et al.* 2015; Nagata *et al.* 2020; Jiang *et al.* 2022). For this purpose, the triple decomposition has been applied to two- or three-dimensional velocity data from direct numerical simulations or experiments with particle image velocimetry. Both experiments and direct numerical simulations have successfully identified shear layers with consistent characteristics (Eisma *et al.* 2015; Watanabe *et al.* 2020; Hayashi *et al.* 2021*a*; Fiscaletti *et al.* 2021; Watanabe *et al.* 2024). Eisma *et al.* (2015) identified a thin layer structure with intense shear in a turbulent boundary layer. Unlike early studies on the shear layers based on the visualisation, the shear component of $\nabla \boldsymbol{u}$ can identify both the location and orientation of shear layers (Watanabe *et al.* 2020). The shear layer location is identified with a scalar quantity related to the intensity of shearing motion, which does not vary with respect to coordinate transformation. For example, the visualisation of the shear intensity in different reference frames is provided in Hayashi *et al.* (2021*a*), where the same shear layer is identified in two frames. This allows us to calculate the statistics conditionally taken in a local reference frame that characterises the shear layer orientation. The mean velocity profiles near the shear layers have been investigated in turbulent boundary layers, jets, mixing layers and HIT (Eisma *et al.* 2015; Watanabe *et al.* 2020; Fiscaletti *et al.* 2021; Hayashi *et al.* 2021*a*). The velocity in the layer-parallel direction exhibits a drastic jump across the shear layer. For HIT and turbulent free shear flows, the Kolmogorov scales characterise the velocity jump and thickness of shear layers (Watanabe *et al.* 2020; Fiscaletti *et al.* 2021; Hayashi *et al.* 2021*a*). In addition, the shear layers have been shown to form in a biaxial strain field. This local flow topology of the shear and strain agrees with Burgers' vortex layer (Davidson 2004). In wall-bounded shear flows, these shear layers possibly separate uniform momentum zones, whose interaction may occur across the shear layers (Eisma *et al.* 2015; Fan *et al.* 2019; Gul *et al.* 2020; Chen *et al.* 2021). Besides these characteristics of shear layers, their roles in turbulence have been explored in recent studies. The viscous dissipation of turbulent kinetic energy primarily occurs within shear layers because the rate-of-strain tensor is dominated by shearing motion (Pirozzoli *et al.* 2010; Nagata *et al.* 2020; Das & Girimaji 2020). Shear layers typically form within a straining flow, which induces vortex stretching, leading to predominant enstrophy production within these layers (Pirozzoli *et al.* 2010; Watanabe *et al.* 2020). Shear layers are inherently unstable, and their roll-up, accompanied by enstrophy amplification, leads to the formation of vortex tubes (Vincent & Meneguzzi 1994; Watanabe & Nagata 2023). This instability is promoted by velocity fluctuations with scales slightly larger than the layer thickness (Watanabe & Nagata 2023). Thus, understanding this instability is crucial for comprehending the scale-by-scale interaction of turbulent motion, which may be connected to the energy cascade process and energy dissipation at the smallest scales. Indeed, Enoki *et al.* (2023) has demonstrated that the velocity fluctuations associated with shearing motion are responsible for the nonlinear energy cascade.

A mean flow pattern around the shear layers reported in the studies mentioned above resembles that observed in a so-called strain eigenframe (Elsinga & Marusic 2010; Elsinga *et al.* 2017; Sakurai & Ishihara 2018). The strain eigenframe is a reference frame defined with the eigenvectors of S_{ij}. The averages in the strain eigenframe are taken from an entire flow field. Nonetheless, the results exhibit a shear layer pattern, as also observed with the averages solely taken for the shear layer region. This also suggests that various turbulence characteristics are explained by the properties of shear layers. For example, the shear layer pattern successfully predicts the $-5/3$ law of an energy spectrum and particle transprot (Elsinga & Marusic 2016; Goudar & Elsinga 2018). The agreement between the

statistics obtained in the strain eigenframe and near the shear layers has been explained by the dominance of shearing motion in turbulence. Analysis of HIT and planar jets has confirmed that shearing motions can appear anywhere in a turbulent flow field. In the near region of the shear layer, shearing motions are highly intense, whereas outside this region, the flow is characterised by moderately intense or weak shear (Watanabe *et al.* 2020; Hayashi *et al.* 2021*a*). Therefore, the mean flow observed in the strain eigenframe is effectively explained by the characteristics of the shear layers. These studies have thus highlighted the importance of shear layers in understanding the behaviour of turbulent flows.

These recent studies of small-scale shear layers motivate further investigation into the characteristics of shear layers in viscoelastic turbulence. Given that shear layers dominate various important phenomena in turbulence, the viscoelastic effects on these layers are expected to elucidate several of the overall modifications induced by viscoelasticity in these flows. Shear layers in viscoelastic turbulence have also been investigated by Horiuti *et al.* (2013). They found that the shear layers become stable due to the tensile forces from the polymers acting on the shear layers. However, these previous investigations focused on flow visualisation techniques. The aim of the present paper is centred on the statistical analysis of the shear layers, facilitated by a recently developed method for detecting shear layers, as discussed earlier. In this work, DNS are carried out to investigate the mean flow properties of shear layers in HIT in a viscoelastic fluid. This fluid consists of a homogeneous dilute solution of long-chained (polymer) molecules dissolved in a Newtonian fluid, which is well described by the FENE-P rheological model (FENE-P: Finitely Extensible Non-linear Elastic constitutive model closed with the Peterlin approximation). Given that the shear layer is a small-scale structure with a thickness close to the Kolmogorov scale, one of the crucial parameters is expected to be the Weissenberg number Wi. The present analysis will show that the shear layers significantly influence the behaviour of polymer molecules in the nearby fluid regions. In addition, the Wi dependence of a mean flow field around the shear layers is shown to be important for the vorticity dynamics and kinetic energy dissipation caused by the polymer molecules. The interest of the present work also lies in elucidating the modified viscous dissipation mechanism in isotropic turbulence for viscoelastic fluids, which can be linked to the mechanism of drag reduction observed in pipes and channels, as discussed in previous studies (Kalelkar *et al.* 2005; Perlekar *et al.* 2006; Cai *et al.* 2010; Ferreira *et al.* 2016).

The paper is organised as follows. Section 2 describes the DNS database used in this study. Section 3 presents the identification method of small-scale shear layers based on the triple decomposition and the conditional averaging procedure used for the statistical analysis. Section 4 discusses local fluid motions described by the triple decomposition and the mean flow field and polymer stress near the shear layers. The role of the shear layers in the vorticity dynamics and kinetic energy dissipation is also revealed based on the mean flow around the shear layers. Finally, the paper is summarised in § 5.

2. DNS of statistically stationary homogeneous isotropic turbulence

The fluid analysed in this study consists of a dilute polymeric solution, formed when a Newtonian solvent carries a very small fraction of long-chain polymer molecules such that interaction between polymer chains is negligible. The fluid is modelled using the Finitely Extensible Non-linear Elastic constitutive model closed with the Peterlin approximation (FENE-P model) (Bird *et al.* 1980). The flow field is incompressible, satisfying the continuity

equation,

$$\frac{\partial u_j}{\partial x_j} = 0, \tag{2.1}$$

and the momentum equations,

$$\frac{\partial u_i}{\partial t} + u_j \frac{\partial u_i}{\partial x_j} = \frac{1}{\rho}\frac{\partial p}{\partial x_i} + \frac{1}{\rho}\frac{\partial \sigma_{ij}}{\partial x_j}, \tag{2.2}$$

where $u_i(\boldsymbol{x}, t)$ is the velocity vector, ρ is the fluid density, and $p(\boldsymbol{x}, t)$ is the pressure. The stress tensor σ_{ij} represents the sum of the Newtonian (solvent) and polymer contributions and is written as

$$\sigma_{ij} = \sigma_{ij}^{[S]} + \sigma_{ij}^{[P]}, \tag{2.3}$$

where the Newtonian stresses are given by,

$$\sigma_{ij}^{[S]} = 2\rho\nu^{[S]} S_{ij}, \tag{2.4}$$

with the Newtonian kinematic viscosity $\nu^{[S]}$. The polymer contribution to the zero-shear-rate kinematic viscosity, $\nu^{[P]}$, can be related to the ratio between the solvent and the total zero-shear-rate viscosity of the solution, $\beta = \nu^{[S]} / \left(\nu^{[P]} + \nu^{[S]}\right)$. The ensembles of polymer chains are represented by a dumbbell model, where two beads are connected by a non-linear spring. These beads represent subsets of chains while the spring accounts for their interactions (Bird *et al.* 1987). The polymeric stresses are then computed as follows:

$$\sigma_{ij}^{[P]} = \frac{\rho\nu^{[P]}}{\tau_P}\left[f(C_{kk})C_{ij} - \delta_{ij}\right], \tag{2.5}$$

where δ_{ij} is the Kronecker symbol, and C_{ij} is the conformation tensor, characterising an ensemble of polymer chains. Here, C_{ij} represents the second-order moment of the end-to-end vector connecting the ends of a polymer chain, normalised by the square of its equilibrium length $\langle r^2\rangle_0$ and is given by

$$C_{ij} = \frac{\langle r_i r_j\rangle}{\langle r^2\rangle_0}, \tag{2.6}$$

where $\langle r^2\rangle$ is the ensemble-averaged squared length of the polymers. The FENE-P model uses the longest relaxation time of the polymer molecules τ_P, and the Peterlin function defined by,

$$f(C_{kk}) = \frac{(L_P)^2 - 3}{(L_P)^2 - C_{kk}}, \tag{2.7}$$

where C_{kk} is the trace of the conformation tensor, and L_P is the maximum extensibility parameter defined as the polymer chain length at the fully extended state normalised by the root-mean-squared end-to-end distance of polymer chain at the equilibrium state. The square root of the trace of the conformation tensor, $\sqrt{C_{kk}}$, represents its normalised extension length. Finally, the conformation tensor is computed by its governing transport equation,

$$\frac{DC_{ij}}{Dt} \equiv \frac{\partial C_{ij}}{\partial t} + u_k\frac{\partial C_{ij}}{\partial x_k} = C_{jk}\frac{\partial u_i}{\partial x_k} + C_{ik}\frac{\partial u_j}{\partial x_k} - \frac{1}{\tau_P}\left[f(C_{kk})C_{ij} - \delta_{ij}\right]. \tag{2.8}$$

In (2.8), the left-hand side represents the material derivative, while the first two terms on the right-hand side represent the polymer stretching/distortion, and the last term is associated with the storage of elastic energy by the polymer molecules.

The present study analyses the DNS database of statistically steady HIT of viscoelastic

fluids described by the FENE-P model in Abreu *et al.* (2022). In the present DNS code, the momentum equations are integrated using pseudo-spectral methods (de-aliased with the 2/3 rule) and a third-order Runge–Kutta scheme for temporal advancement. Specifically, for (2.2), the diffusive terms involving the shear and polymer stress tensors are computed in Fourier space, while the non-linear terms are evaluated in physical space (using de-aliasing). Similarly, for the conformation tensor, temporal advancement employs the same Runge–Kutta scheme as used for the momentum equations, with all terms computed using pseudo-spectral methods for spatial differencing, except for the convective term. This term is calculated using the central-differences algorithm proposed by Vaithianathan *et al.* (2006), based on the Kurganov–Tadmor method, which ensures that the conformation tensor remains symmetric and positive definite, avoiding the need to add artificial diffusion in (2.8). The statistically steady state is achieved by using a forcing scheme (Alvelius 1999). More details of the DNS code are given in Ferreira *et al.* (2016), Silva *et al.* (2018), Abreu *et al.* (2022) and references therein. The present algorithm and its implementation have been extensively validated in a series of papers, beginning with Valente *et al.* (2014*b*). Moreover, the values of τ_p, L_p and β used in this study roughly match those in the experimental study by Ouellette *et al.* (2009). The experiments utilised polyacrylamide in concentration up to 45 p.p.m. in weight (equivalent to $\beta \geqslant 0.8$), which is considered dilute. The validations and comparisons with experiments and other DNS were reported in our previous studies (Valente *et al.* 2014*b*; Guimarães *et al.* 2020, 2022, 2023). Additionally, it is also important to note that the Kolmogorov scale is much larger than the maximum extension of the polymer molecules (Valente *et al.* 2014*b*).

Table 1 summarises the physical parameters of the DNS databases, which are the same as in Abreu *et al.* (2022) and include a reference Newtonian DNS and a total of 4 viscoelastic simulations. The simulations use a triply periodic domain of sizes $(2\pi \times 2\pi \times 2\pi)$ and $N^3 = 768^3$ collocation points. The statistics reported in this work are obtained with the combined ensemble and volume averages, denoted by $\langle f \rangle$. The kinematic viscosity of the solvent is $\nu^{[S]} = 0.0023$ in all simulations, and the viscoelastic simulations differ by the value of the maximum relaxation time of the polymer molecules, τ_P, which varies between 0.025 and 0.2. The ratio between the solvent and the total zero-shear-rate viscosities of the solution and the maximum extensibility of the polymers are equal to $\beta = 0.8$ and $(L_P)^2 = 100^2$, respectively, in all the viscoelastic simulations. The Kolmogorov length, velocity and time scales are defined as $\eta = (\nu^{[S]}/\langle\varepsilon_\nu\rangle^{1/3})^{3/4}$, $u_\eta = (\nu^{[S]}\langle\varepsilon_\nu\rangle)^{1/4}$ and $\tau_\eta = (\nu^{[S]}/\langle\varepsilon_\nu\rangle)^{1/2}$, respectively, where $\varepsilon_\nu = 2\nu^{[S]}S_{ij}S_{ij}$ is the solvent viscous dissipation rate of kinetic energy. Notice that the present definitions for the Kolmogorov (length, velocity and time) scales characterise the smallest existing scales of motion for the solvent. However, it is clear that these are not the characteristic scales of motion for viscoelastic turbulent flows in the classical sense. Specifically, the statistics of the flow do not collapse when normalised by these scales (Valente *et al.* 2014*b*). The Weissenberg number is $Wi = \tau_P/\tau_\eta$, which is the time scale ratio between the maximum relaxation time of the polymer molecules and the Kolmogorov time scale. The range of values of Wi used in these simulations covers the three regimes previously observed in isotropic turbulence of viscoelastic fluids as described in previous studies (Valente *et al.* 2014*b*; Ferreira *et al.* 2016). For very low Wi, viscoelastic effects manifest as an additional (small) viscosity without any other additional effects. At higher Wi values, the viscoelastic effects significantly alter the energy cascade, causing deviations of the kinetic energy spectra from the classical $-5/3$ Kolmogorov–Obukhov law. At even higher Wi, the polymers and solvent become decoupled, and the $-5/3$ law is observed once again. The transition between the latter two regimes is observed at approximately $Wi = 2$ (Ferreira *et al.* 2016). The turbulent Reynolds number $Re_\lambda = u_0\lambda/\nu^{[S]}$ is defined with the root-mean-squared (r.m.s.) value of velocity fluctuations of HIT, $u_0 = \sqrt{\langle u^2\rangle + \langle v^2\rangle + \langle w^2\rangle/3}$, and

Table 1: DNS databases of homogeneous isotropic turbulence in Newtonian (Newt.) and viscoelastic fluids: Weissenberg number (Wi); the maximum relaxation time of the polymer molecules (τ_P); turbulent Reynolds number (Re_λ); r.m.s. velocity fluctuations (u_0); solvent mean viscous dissipation rate ($\langle\varepsilon_s\rangle$); polymer mean dissipation rate ($\langle\varepsilon_p\rangle$); dissipation reduction (DR); Taylor microscale (λ); Kolmogorov micro-scale (η); Kolmogorov time-scale (τ_η); Kolmogorov velocity-scale (u_η); the maximum effective wavenumber normalised by the Kolmogorov scale ($k_{max}\eta$).

Wi	τ_P	Re_λ	u_0	$\langle\varepsilon_s\rangle$	$\langle\varepsilon_p\rangle$	DR %	λ ($\times10^{-1}$)	η ($\times10^{-3}$)	τ_η ($\times10^{-2}$)	u_η ($\times10^{-1}$)	$k_{max}\eta$
(Newt.)	–	181	2.6	9.9	–	–	1.6	5.9	1.5	3.9	1.5
1.3	0.025	222	2.7	7.34	2.66	27	1.9	6.5	1.9	3.5	1.7
2.0	0.05	280	2.6	3.94	6.06	61	2.5	7.5	2.5	3.1	1.9
3.0	0.1	363	2.5	2.04	7.96	80	3.3	8.8	3.3	2.6	2.2
4.6	0.2	397	2.3	1.13	8.87	89	3.9	10.0	4.4	2.3	2.6

the Taylor micro-scale $\lambda = \sqrt{15\nu^{[S]}u_0/\langle\varepsilon_\nu\rangle}$. The table also shows the mean dissipation rates caused by the solvent and by the polymers, denoted as $\langle\varepsilon_s\rangle$ and $\langle\varepsilon_p\rangle = \langle\sigma_{ij}^{[P]}S_{ij}\rangle$, respectively. Additionally, it includes the drag reduction (also referred to as dissipation reduction), which is defined as DR $= \varepsilon_p/(\varepsilon_s + \varepsilon_p)$, following the definitions used in Cai *et al.* (2010) and Ferreira *et al.* (2016). The results in table 1 indicate that DR values of approximately 80% are observed for the viscoelastic simulations at the highest value of Wi. The maximum effective wavenumber k_{max} normalised by η is higher than 1.5 for all the simulations, attesting that the smallest scales of motion are always finely resolved. The ensemble averages are taken for 10 snapshots saved with a time interval of the Kolmogorov time scale. To estimate statistical errors, we employ a method based on subdividing the computational domain. Specifically, the entire computational domain is divided into two equal halves, generating two separate datasets. We then calculate statistical quantities independently within each of these datasets. The measure of statistical errors for a given statistical quantity is determined by comparing its value as calculated within each half-domain against the value obtained for the whole domain. As shown below, the statistical errors are negligible for the shear layer analysis.

3. Statistical analysis of small-scale shear layers

3.1. *The triple decomposition*

The triple decomposition of the velocity gradient tensor is used to investigate shearing motion in turbulence (Kolář 2007). Several algorithms have been proposed for the triple decomposition (Kolář 2007; Nagata *et al.* 2020; Hayashi *et al.* 2021*a*; Kronborg & Hoffman 2023). The present study uses the one presented in Hayashi *et al.* (2021*a*). The explanation given below follows these early studies of the triple decomposition, which can be referred to for the details of the physical meaning and algorithm of the decomposition.

The triple decomposition splits $\nabla\boldsymbol{u}$ into three components of *i)* shear, *ii)* rigid-body rotation and *iii)* irrotational strain (elongation) as $\nabla\boldsymbol{u} = \nabla\boldsymbol{u}_S + \nabla\boldsymbol{u}_R + \nabla\boldsymbol{u}_E$, where S, R and E stands for shear, rotation and elongation, respectively. The decomposition formula below has to be applied in a specific reference frame, called *basic reference frame*. The basic reference frame is chosen from many reference frames defined with three sequential rotational transformations

$\boldsymbol{Q}(\theta_1, \theta_2, \theta_3)$:

$$\boldsymbol{Q} = \begin{pmatrix} \cos\theta_1\cos\theta_2\cos\theta_3 - \sin\theta_1\sin\theta_3 & \sin\theta_1\cos\theta_2\cos\theta_3 + \cos\theta_1\sin\theta_3 & -\sin\theta_2\cos\theta_3 \\ -\cos\theta_1\cos\theta_2\sin\theta_3 - \sin\theta_1\cos\theta_3 & -\sin\theta_1\cos\theta_2\sin\theta_3 + \cos\theta_1\cos\theta_3 & \sin\theta_2\sin\theta_3 \\ \cos\theta_1\sin\theta_2 & \sin\theta_1\sin\theta_2 & \cos\theta_2 \end{pmatrix} \tag{3.1}$$

with angles $0° \leqslant \theta_1 \leqslant 180°$, $0° \leqslant \theta_2 \leqslant 180°$ and $0° \leqslant \theta_3 \leqslant 90°$. The reference frame of DNS, $\boldsymbol{x}$, is transformed to the rotated reference frame $\boldsymbol{x}^*$ as $\boldsymbol{x}^* = \boldsymbol{Q}\boldsymbol{x}$. In this frame, the velocity gradient tensor is expressed as $(\nabla \boldsymbol{u})^* = \boldsymbol{Q}\,(\nabla \boldsymbol{u})\,\boldsymbol{Q}^T$. Here, superscript $*$ represents a quantity in the rotated reference frame. The basic reference frame assumes that an interaction scalar, $I^* = |\Omega^*_{12}S^*_{12}| + |\Omega^*_{23}S^*_{23}| + |\Omega^*_{31}S^*_{31}|$, becomes the largest among all reference frames. The basic reference frame can be determined by evaluating I^* in many reference frames for discrete sets of $(\theta_1, \theta_2, \theta_3)$. First, I^* is evaluated for $\boldsymbol{x}^* = \boldsymbol{Q}\boldsymbol{x}$ with

$$\theta_1 = 0, 45°, ..., 180°, \tag{3.2}$$

$$\theta_2 = 0, 45°, ..., 180°, \tag{3.3}$$

$$\theta_3 = 0, 45°, 90°. \tag{3.4}$$

From these sets of $(\theta_1, \theta_2, \theta_3)$, one can find the angles that provide the largest I^*. These angles are denoted by $(\theta_1^{(1)}, \theta_2^{(1)}, \theta_3^{(1)})$. Then, the largest I^* is searched for $\boldsymbol{x}^* = \boldsymbol{Q}\boldsymbol{x}$ with

$$\theta_i = \theta_i^{(min)}, \theta_i^{(min)} + 15°, ..., \theta_i^{(max)}, \tag{3.5}$$

$$\theta_i^{(min)} = \theta_i^{(1)} - 45°/2, \tag{3.6}$$

$$\theta_i^{(max)} = \theta_i^{(1)} + 45°/2. \tag{3.7}$$

for $i = 1, 2$ and 3. Again, the angles for the largest I^* are denoted by $(\theta_1^{(2)}, \theta_2^{(2)}, \theta_3^{(2)})$. Finally, the basic reference frame is determined with the angles with the largest I^* among

$$\theta_i = \theta_i^{(min)}, \theta_i^{(min)} + 5°, ..., \theta_i^{(max)}, \tag{3.8}$$

$$\theta_i^{(min)} = \theta_i^{(2)} - 15°/2, \tag{3.9}$$

$$\theta_i^{(max)} = \theta_i^{(2)} + 15°/2. \tag{3.10}$$

The angles with the largest I^* are denoted by $(\theta_1^{(B)}, \theta_2^{(B)}, \theta_3^{(B)})$, by which the basic reference frame is obtained with $\boldsymbol{x}^{(B)} = \boldsymbol{Q}(\theta_1^{(B)}, \theta_2^{(B)}, \theta_3^{(B)})\boldsymbol{x}$. The velocity gradient tensor in the basic reference frame is also calculated as $(\nabla \boldsymbol{u})^{(B)} = \boldsymbol{Q}\,(\nabla \boldsymbol{u})\,\boldsymbol{Q}^T$. Then, the triple decomposition calculates the decomposed tensors as

$$(\nabla \boldsymbol{u}_{RES})^{(B)}_{ij} = \mathrm{sgn}\left[(\nabla \boldsymbol{u})^{(B)}_{ij}\right] \min\left[\left|(\nabla \boldsymbol{u})^{(B)}_{ij}\right|, \left|(\nabla \boldsymbol{u})^{(B)}_{ji}\right|\right], \tag{3.11}$$

$$(\nabla \boldsymbol{u}_S)^{(B)}_{ij} = (\nabla \boldsymbol{u})^{(B)}_{ij} - (\nabla \boldsymbol{u}_{RES})^{(B)}_{ij}, \tag{3.12}$$

$$(\nabla \boldsymbol{u}_R)^{(B)}_{ij} = \left[(\nabla \boldsymbol{u}_{RES})^{(B)}_{ij} - (\nabla \boldsymbol{u}_{RES})^{(B)}_{ji}\right]/2, \tag{3.13}$$

$$(\nabla \boldsymbol{u}_E)^{(B)}_{ij} = \left[(\nabla \boldsymbol{u}_{RES})^{(B)}_{ij} + (\nabla \boldsymbol{u}_{RES})^{(B)}_{ji}\right]/2, \tag{3.14}$$

for $i, j = 1, 2$ and 3, where sgn is a sign function. These tensors are evaluated in the basic reference frame. Finally, the decomposed tensors in the original reference frame, $\nabla \boldsymbol{u}_S$, $\nabla \boldsymbol{u}_R$ and $\nabla \boldsymbol{u}_E$, are calculated by applying the inverse transformation of $\boldsymbol{Q}(\theta_1^{(B)}, \theta_2^{(B)}, \theta_3^{(B)})$ to the corresponding tensors in the basic reference frame. The intensities of three motions are evaluated as $I_\alpha = \sqrt{2(\nabla \boldsymbol{u}_\alpha)_{ij}(\nabla \boldsymbol{u}_\alpha)_{ij}}$ for $\alpha = S, R$ and E. The interaction scalar I^* represents an effective pure shearing motion extracted by the decomposition fomula. The effect of the

extraction of the shear tensor $\nabla \boldsymbol{u}$ is also maximized in the basic reference frame with the largest I^*. This is because the norm of $\nabla \boldsymbol{u}$ is written as $||(\nabla \boldsymbol{u})^*||^2 = ||(\nabla \boldsymbol{u}_{RES})^*||^2 + 4I^*$ in any reference frames (Kolář 2007). The original triple decomposition is fomulated as an optimisation problem of searching the basic reference frame. Later, it is shown that the solution of this maximisation problem for I^* corresponds to the standardised real Schur form of the velocity gradient tensor (Kronborg & Hoffman 2023).

3.2. *Conditional statistics of small-scale shear layers*

In the present work, shear layers are statistically analysed by detecting them through the triple decomposition formalism described above. Within this framework, statistics are conditionally calculated in a local reference frame defined for each detected shear layer, with the same method as outlined in Watanabe & Nagata (2022) and Watanabe & Nagata (2023). The detailed algorithm for the conditional averages has been described in these papers (and references therein), and here only a brief explanation is given on the procedure used to evaluate the statistics of these shear layers.

The small-scale shear layers arising from turbulent velocity fluctuations can be detected with the shear intensity I_S. The shear layer locations are identified with the local maxima of I_S, which the Hessian matrix of I_S can uniquely determine. The gradient of I_S is denoted by $\partial_x I_S = \partial I_S/\partial x$, $\partial_y I_S = \partial I_S/\partial y$ and $\partial_z I_S = \partial I_S/\partial z$. The shear layer analysis is conducted for the local maxima of I_S which satisfy

$$\partial_x I_S(x-\Delta x, y, z) > 0, \quad \partial_x I_S(x+\Delta x, y, z) < 0, \tag{3.15}$$

$$\partial_y I_S(x, y-\Delta y, z) > 0, \quad \partial_y I_S(x, y+\Delta y, z) < 0, \tag{3.16}$$

$$\partial_z I_S(x, y, z-\Delta z) > 0, \quad \partial_z I_S(x, y, z+\Delta z) < 0, \tag{3.17}$$

with Δx, Δy and Δz ranging between 0 and 2Δ, where Δ is the computational grid size. These conditions follow Hayashi *et al.* (2021*a*) and discard the local maxima of I_S associated with noise-like patterns from the analysis.

For each detected shear layer, a local reference frame $(\zeta_1, \zeta_2, \zeta_3)$ is introduced for the conditional statistics. This reference frame is defined with the shear orientation and referred to as a shear coordinate (latter shown as Fig. 6). The procedure to determine the shear coordinate follows Watanabe *et al.* (2020) and is briefly explained here. An example of a flow field observed in the shear coordinate is also presented in § 4.3. The velocity vector in this reference frame is denoted by $(u_{\zeta_1}, u_{\zeta_2}, u_{\zeta_3})$. The shear coordinate assumes that the shear is predominantly represented by $\partial u_{\zeta_3}/\partial \zeta_2$. The unit vectors in the ζ_1, ζ_2 and ζ_3 directions are denoted by $\boldsymbol{n}_{\zeta_1}$, $\boldsymbol{n}_{\zeta_2}$ and $\boldsymbol{n}_{\zeta_3}$, respectively. First, $\boldsymbol{n}_{\zeta_1}$ is taken in the direction of the shear vorticity vector $(\boldsymbol{\omega}_S)_i = \epsilon_{ijk}(\nabla \boldsymbol{u}_S)_{jk}$ as $\boldsymbol{n}_{\zeta_1} = \boldsymbol{\omega}_S/|\boldsymbol{\omega}_S|$, where ϵ_{ijk} is the Levi-Civita symbol. The other two unit vectors are determined in a similar method used to identify the basic reference frame, by which the shear coordinate is chosen from $N_n = 4000$ orthogonal coordinates where the x component of $\boldsymbol{n}_2$ is given by $(\boldsymbol{n}_2)_x = 2(n/N_n - 0.5)$ with an integer $n = 0, ..., N_n$. For each value of n, $\boldsymbol{n}_2$ and $\boldsymbol{n}_3$ can be determined by the following conditions: $\boldsymbol{n}_i \cdot \boldsymbol{n}_j = 0$ for $i \neq j$; $|\boldsymbol{n}_i| = 1$ for $i = 1, 2$ and 3; $\boldsymbol{n}_{\zeta_1} = \boldsymbol{\omega}_S/|\boldsymbol{\omega}_S|$. The coordinate transformation tensor from (x, y, z) to the new reference frame can be obtained with $\boldsymbol{n}_{\zeta_1}$, $\boldsymbol{n}_{\zeta_2}$ and $\boldsymbol{n}_{\zeta_3}$. Then, the shear component $\nabla \boldsymbol{u}_S$ evaluated in the new reference frame is denoted by $(\nabla \boldsymbol{u}_S)^{(n)}$. The shear coordinate is determined with n that yields the largest value of $(\nabla \boldsymbol{u}_S)^{(n)}_{32}$.

For each shear layer, variables defined on the DNS grid are interpolated on the shear coordinate, which is also represented by discrete points. Various vectors and tensors are evaluated in the shear coordinate, where the components are denoted with subscript ζ_i, e.g. ω_{ζ_i} for the vorticity vector and $\sigma^{[P]}_{\zeta_i\zeta_j}$ for the polymer stress tensor. The interpolation is repeated for all detected shear layers. Finally, the ensemble averages of the shear layers are

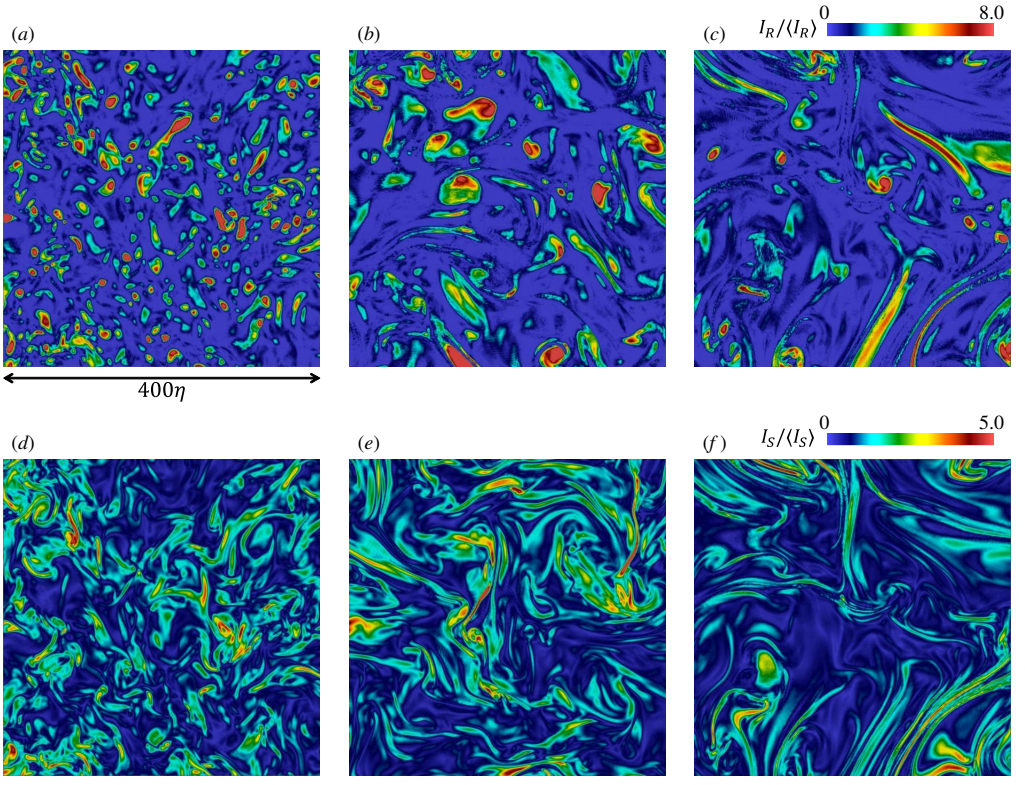

Figure 1: Two-dimensional profiles of intensities of (*a*-*c*) rigid-body rotation and (*d*-*f*) shear: (*a*, *d*) Newtonian case; viscoelastic cases with (*b*, *e*) $Wi = 2.0$ and (*c*, *f*) $Wi = 4.6$. Only a small part of the computational domain ($400\eta \times 400\eta$) is shown here.

taken as functions of $(\zeta_1, \zeta_2, \zeta_3)$. This average is denoted by $\overline{f}$. In all cases, the number of samples utilised for ensemble averaging exceeds 3×10^5, which is in line with similar shear layer analyses conducted for turbulent jets (Hayashi *et al.* 2021*a*,*b*). The statistical convergence test in Hayashi *et al.* (2021*b*) indicates that 3×10^5 samples are sufficient to yield reliable statistical data for shear layers. To further assess the statistical accuracy, additional examinations of statistical errors are conducted for the present DNS databases below.

The present study focuses on examining the mean properties of shear layers. Watanabe & Nagata (2023) conducted an investigation into the characteristics of individual shear layers in Newtonian HIT. They revealed that the probability density functions (p.d.f.s) of various properties of shear layers, such as thickness, velocity jump and local Reynolds number, typically exhibit a single peak. This peak aligns with the shear layer charcteristics deduced from the mean flow pattern around the shear layers in other studies (Watanabe *et al.* 2020; Hayashi *et al.* 2021*a*; Fiscaletti *et al.* 2021). Given these findings, employing ensemble averages of shear layers emerges as a valuable approach to explore the characteristics of these structures.

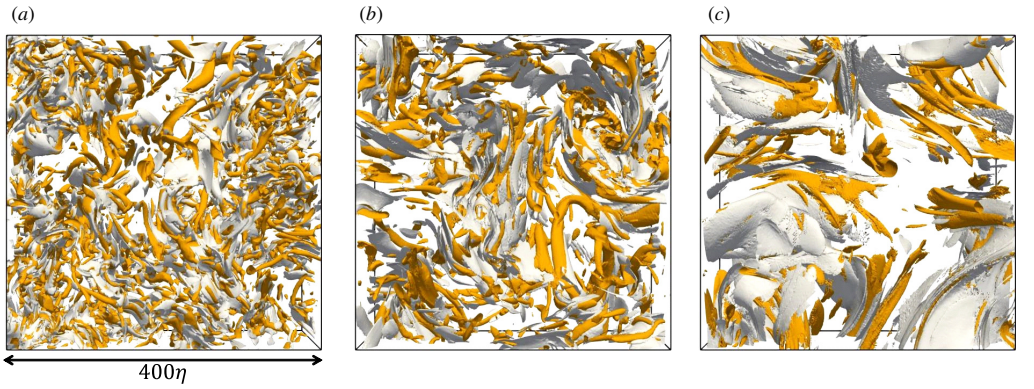

Figure 2: Shear layers (white) and vortex tubes (orange), which are visualised by the isosurfaces of intensities of shear, $I_S = 2\langle I_S \rangle$, and rigid-body rotation, $I_R = 4\langle I_R \rangle$: (*a*) Newtonian case; viscoelastic cases with (*b*) $Wi = 2.0$ and (*c*) $Wi = 4.6$. Only a small part of the computational domain ($400\eta \times 400\eta \times 150\eta$) is shown here.

4. Results and discussion

4.1. *Shear and rotating motions in viscoelastic turbulence*

Figure 1 shows contours of the intensities of shear and rigid-body rotation, I_S and I_R, on two-dimensional planes in the Newtonian case and viscoelastic cases with $Wi = 2.0$ and 4.6. All figures show regions with $(400\eta)^2$. These quantities can be used to detect shear layers and vortex tubes in turbulence (Nagata *et al.* 2020). Circular patterns of large I_R are the cross-sections of vortex tubes, while their long patterns are related to the axes of in-plane vortex tubes. On the other hand, large I_S is often concentrated in thin layers, which are the shear layers due to turbulent fluctuations. A comparison between the Newtonian and viscoelastic cases shows that the geometry of these structures changes as Wi increases. Here, the shear layers in the viscoelastic simulations are longer than in the Newtonian case. Additionally, the vortex tubes appear less frequently in the viscoelastic case than in the Newtonian case. Figure 2 displays the iso-surfaces of I_S and I_R in a region of $400\eta \times 400\eta \times 150\eta$. As also shown in the two-dimensional visualisation, the aspect ratio of shear layers becomes large as Wi increases. The instability of the shear layers results in the formation of vortex tubes (Vincent & Meneguzzi 1994; Watanabe & Nagata 2023; Watanabe 2024), and their length scales are related to each other. Because of the larger size of the shear layers at higher Wi, the size of the vortex tubes also increases in the viscoelastic simulations.

Figure 3 shows the temporal evolution of shear layers and vortex tubes in a Newtonian fluid over a duration of $3\tau_\eta$. The sequence progresses from figure 3(*a*) to figure 3(*d*) at constant intervals of τ_η. During this time, the formation of vortices from shear layers is distinctly observable. In figure 3(*a*), a shear layer, labeled 'S,' already encompasses a vortex, 'V1,' which has formed within it. As this layer evolves, additional vortices 'V2' and 'V3' emerge from the same layer, as seen in figure 3(*b*, *c*). Eventually, this shear layer fragments and partially disappears in figure 3(*d*). Such vortex formation processes in shear layers are explained by the shear instability and are also documented in other studies (Vincent & Meneguzzi 1994; Watanabe *et al.* 2020; Watanabe & Nagata 2023).

Figure 4 presents a similar visualisation but over a longer duration of $7\tau_\eta$ for the viscoelastic simulation with $Wi = 4.6$. Even in the viscoelastic case, the vortex formation occurs: a shear layer marked as 'S' produces a vortex 'V.' However, this process unfolds more gradually compared to the Newtonian case. Additionally, many shear layers in the viscoelastic fluid

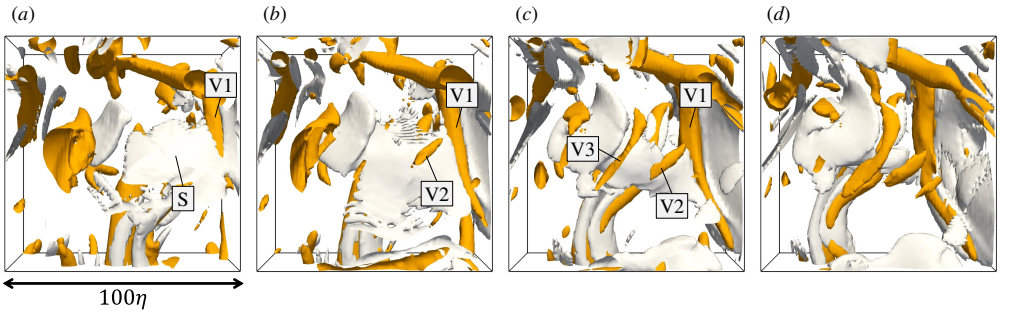

Figure 3: Temporal evolution of shear layers (white) and vortex tubes (orange) for the reference Newtonian simulation, which are visualised by the same isosurfaces as those in figure 2(*a*). The progression from (*a*) to (*d*) represents the advancement of time in intervals of the Kolmogorov time scale, τ_η. Only a small part of the computational domain ($100\eta \times 100\eta \times 50\eta$) is shown here.

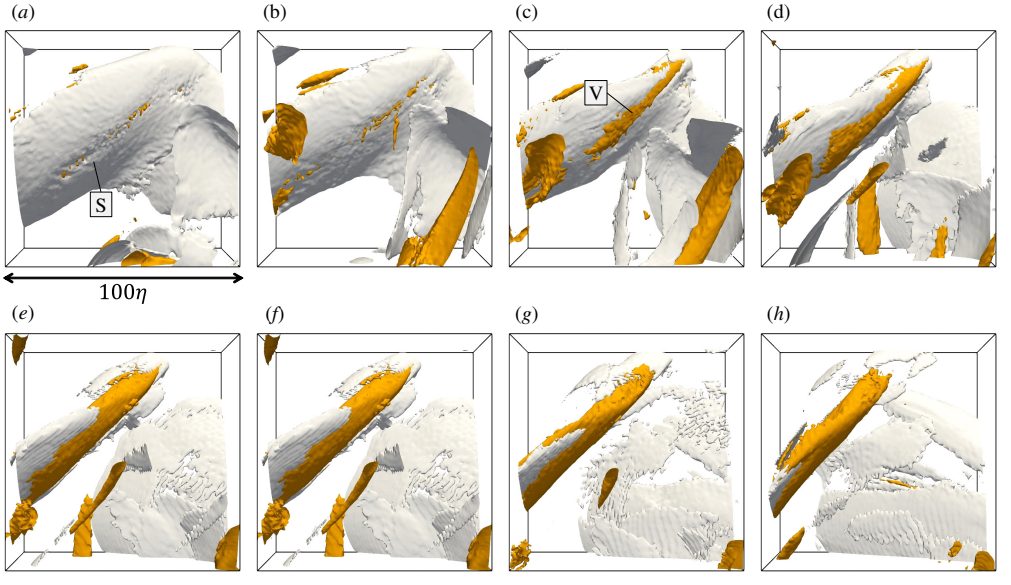

Figure 4: The same as figure 3 but for the viscoelastic simulation with $Wi = 4.6$. Temporal evolution is visualised over $7\tau_\eta$ from (*a*) to (*h*).

do not readily form vortices, in contrast to the vortex generation within shear layers in the Newtonian fluid. Horiuti *et al.* (2013) has demonstrated that shear layers in viscoelastic turbulence tend to stabilise due to the tensile forces exerted by polymers on the shear layers by conducting DNS with the Johnson–Segalman model for the polymer stress. This stabilisation inhibits the fragmentation of large shear layers into smaller ones, resulting in shear layers with a low aspect ratio in Newtonian turbulence. Consequently, this inhibited instability in viscoelastic fluids accounts for the observation of larger and flatter shear layers, as shown in figure 2(*c*).

Figure 5 shows the probability density functions (p.d.f.s) of I_S, I_R and I_E normalised by the Kolmogorov time scale. The distribution of the p.d.f.s is similar to those in turbulent jets and HIT of Newtonian fluids (Hayashi *et al.* 2021*a*). The peaks of the p.d.f.s appear at

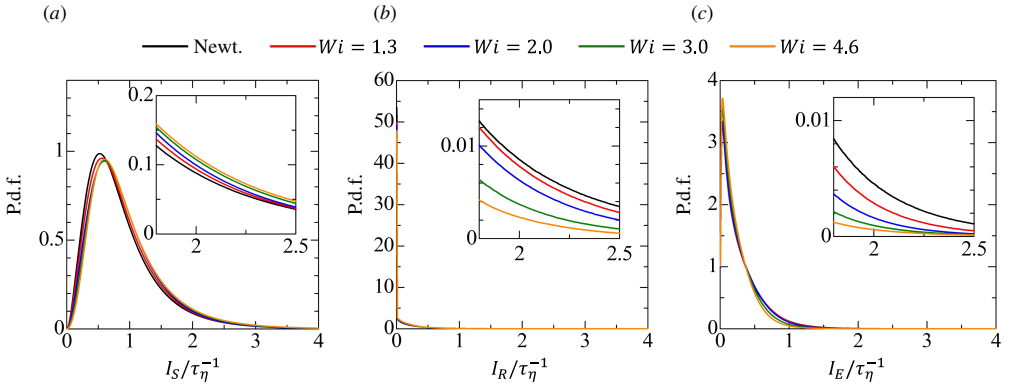

Figure 5: Probability density functions (p.d.f.s) of intensities of (a) shear, (b) rigid-body rotation and (c) elongation normalised by the Kolmogorov time scale τ_η. The insets show the p.d.f.s with moderately large values of the intensities.

$I_S/\tau_\eta^{-1} \approx 0.5$, $I_R = 0$ and $I_E/\tau_\eta^{-1} \approx 0.03$, indicating that most of the flow is dominated by shearing motion. This is also confirmed in figure 1, where I_S has non-zero values even if it is small while $I_R \approx 0$ is observed except for regions occupied by vortex tubes. Thus, rigid-body rotation and elongation are highly intermittent in space. The insets show the p.d.f.s for moderately large intensities of these motions. As Wi increases, the p.d.f. for large I_S increases and those for large I_R and I_E decrease. Therefore, shearing motion becomes more dominant in local fluid motion than the other motions in a viscoelastic fluid. The vorticity vector can be decomposed into two components of shear and rigid-body rotation as $\boldsymbol{\omega} = \boldsymbol{\omega}_S + \boldsymbol{\omega}_R$ with $(\boldsymbol{\omega}_S)_i = \epsilon_{ijk}(\nabla \boldsymbol{u}_S)_{jk}$ and $(\boldsymbol{\omega}_R)_i = \epsilon_{ijk}(\nabla \boldsymbol{u}_R)_{jk}$ (Kolář 2007). The structures related to $\boldsymbol{\omega}_S$ and $\boldsymbol{\omega}_R$ are shear layers and vortex tubes, respectively (Eisma *et al.* 2015; Nagata *et al.* 2020; Fiscaletti *et al.* 2021). Therefore, the Wi dependence of the p.d.f.s suggests that the vorticity is more related to shear layers than vortex tubes in viscoelastic turbulence. DNS of viscoelastic turbulence has also shown that more sheet-like structures are identified in visualisation with vorticity as Wi increases (Watanabe & Gotoh 2014; Ferreira *et al.* 2016). This tendency is well explained by the dominance of shearing motion over rotating motion at high Wi because the shear vorticity $\boldsymbol{\omega}_S$ becomes more important in the total vorticity $\boldsymbol{\omega}$ as Wi increases.

4.2. *Mean flow field of small-scale shear layers*

This section discusses the mean flow field evaluated in the shear coordinate, sketched in figure 6(a). Shearing motion is not usually observed in the reference frame of DNS because the shear layers have no preference in the orientation with respect to x, y and z. However, in the local shear coordinates, a local shear-flow pattern is easily observed in the ζ_2–ζ_3 plane. This is confirmed in figure 6(b), where a flow around one of the shear layers is visualised on the ζ_2–ζ_3 plane at $\zeta_1 = 0$. The thin shear layer with large I_S is extended in the ζ_3 direction. Flows in the $\pm\zeta_3$ directions are observed on the sides of the shear layer, generating shear in the layer structure. The conditional averages taken as functions of $(\zeta_1, \zeta_2, \zeta_3)$ reveal the mean flow characteristics of the shear layers shown in figure 6(b).

Figure 7 shows the mean flow field around the shear layer with the mean shear intensity $\overline{I_S}$ and mean velocity vectors on the visualised planes for the Newtonian case. The three planes intersecting the centre of the shear layers are visualised in each figure. Large $\overline{I_S}$ is observed in a layer which is thin in the ζ_2 direction and long in the other two directions. On the ζ_2–ζ_3 plane, the mean flows in the ζ_3 and $-\zeta_3$ directions appear for $\zeta_2 > 0$ and $\zeta_2 < 0$, respectively,

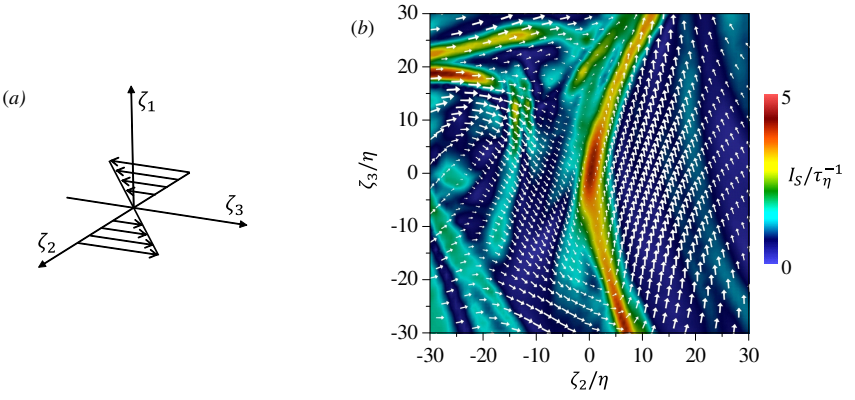

Figure 6: (a) A schematic of a shear coordinate. (b) A shear layer observed in the shear coordinate for $Wi = 3.0$. The shear intensity I_S and two-dimensional velocity vectors are shown on the ζ_2–ζ_3 plane at $\zeta_1 = 0$. The relative velocity vectors to the velocity at $(\zeta_1, \zeta_2, \zeta_3) = (0, 0, 0)$ are shown here. The length of the vectors corresponds to the vector magnitude.

representing local shearing motion. The mean velocity vectors on the ζ_1–ζ_2 plane exhibits a biaxial strain with stretching in the ζ_1 direction and compression in the ζ_2 direction, which are confirmed by $\partial\overline{u_{\zeta_1}}/\partial\zeta_1 > 0$ and $\partial\overline{u_{\zeta_2}}/\partial\zeta_2 < 0$. The ζ_1–ζ_3 plane is parallel to the shear layer, and the ζ_3 dependence of the mean flow on this plane is relatively weak compared to the dependence in the other directions. These mean flow patterns are independent of flows and Reynolds numbers under Kolmogorov normalisation (Watanabe *et al.* 2020; Fiscaletti *et al.* 2021; Hayashi *et al.* 2021*a*), and the present results agree with these previous studies.

Figures 8 and 9 present the mean flows near the shear layers in the viscoelastic simulations with $Wi = 2.0$ and 4.6. The shear and straining flows observed on the ζ_2–ζ_3 and ζ_1–ζ_2 planes also appear in the viscoelastic cases. However, the large-$\overline{I_S}$ region is extended for larger $|\zeta_1|$ and $|\zeta_3|$ as Wi increases from the Newtonian case. The layer thickness in the ζ_2 direction is thinner in the viscoelastic cases than in the Newtonian case. Therefore, the aspect ratio of the shear layers increases in the viscoelastic turbulence, as also observed for the visualised shear layers in figure 2.

Figures 10 and 11 present the three-dimensional visualisations of the streamlines of mean flow around shear layers for Newtonian and viscoelastic cases, respectively. A shear flow with compressive motion in the direction normal to the layer is observed on either side of the shear layer, as indicated by the streamlines contracting toward the layer. Furthermore, the streamlines within the shear layer are oriented in the ζ_1 direction, where extensive strain facilitates the stretching of shear vorticity. The inherent vorticity of the shear layer with a finite aspect ratio causes the streamlines to exhibit partially rotating patterns at the edges of the shear layers. In fact, the mean profile of the intensity of rigid-body rotation supports the presence of vortices associated with rigid-body rotation at the edges of the shear layer (Watanabe & Nagata 2022). The observed flow pattern, characterised by a combination of shear, stretching in the ζ_1 direction, and compression in the ζ_2 direction, is typical of small-scale shear layers in turbulent flows. This pattern is crucial in defining the structures within turbulent flows in terms of fluid particle motion.

Because of the shear and strain acting on the layer, mean velocity jumps are observed for $\overline{u_{\zeta_1}}$ on the ζ_1 axis and $\overline{u_{\zeta_2}}$ and $\overline{u_{\zeta_3}}$ on the ζ_2 axis. The corresponding mean velocity profiles are shown in figure 12 for all simulations. For $\overline{u_{\zeta_1}}$, the mean velocity difference between $\zeta_1 > 0$ and $\zeta_1 < 0$ becomes large as Wi increases. However, the velocity jump is observed

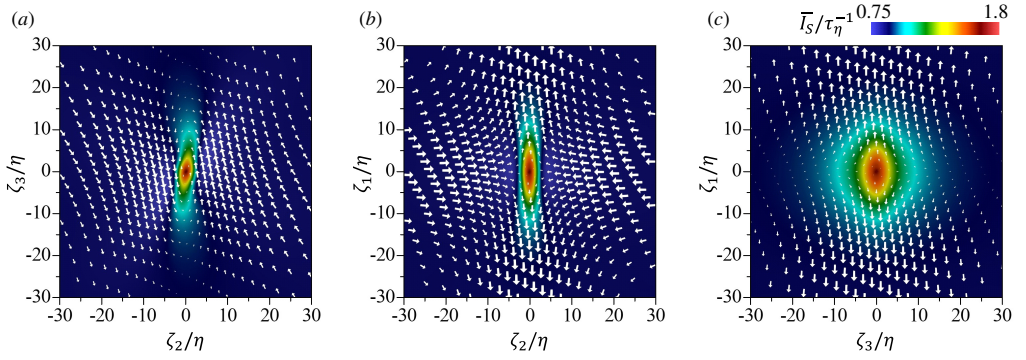

Figure 7: Mean shear intensity $\overline{I_S}$ and mean velocity vectors on (a) ζ_2–ζ_3 plane at $\zeta_1 = 0$, (b) ζ_1–ζ_2 plane at $\zeta_3 = 0$ and (c) ζ_1–ζ_3 plane at $\zeta_2 = 0$ for the Newtonian case. The length of the vectors corresponds to the vector magnitude in each figure.

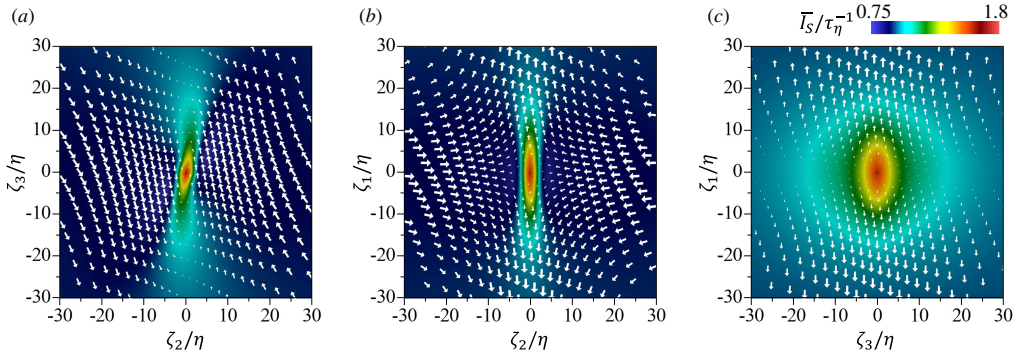

Figure 8: The same as figure 7 but for $Wi = 2.0$.

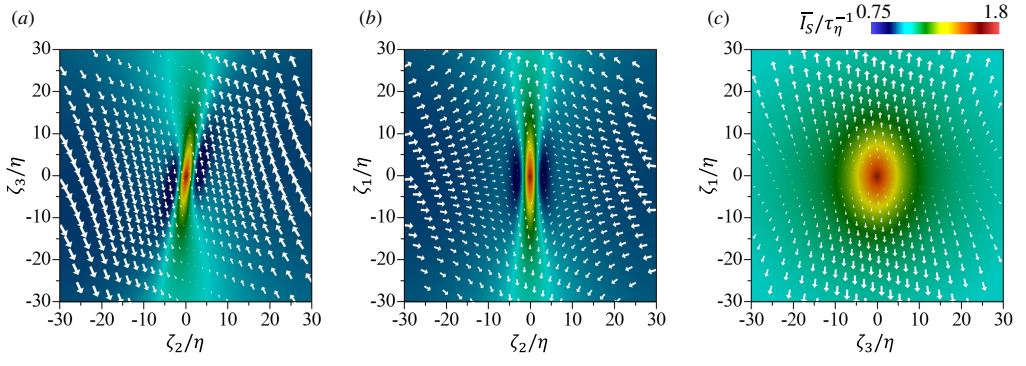

Figure 9: The same as figure 7 but for $Wi = 4.6$.

over a longer distance at higher Wi, resulting in smaller $\partial\overline{u_{\zeta_1}}/\partial\zeta_1$ within the shear layer. For $\overline{u_{\zeta_2}}$ and $\overline{u_{\zeta_3}}$, the mean velocity differences also increase with Wi. However, viscoelasticity has virtually no effect on the mean velocity gradient within the shear layer.

Figure 13 presents an analysis of statistical errors by displaying the mean velocity and shear intensity profiles across the shear layers, as derived from two separate datasets described in § 3.2. Each dataset represents half of the computational domain. The comparison of these

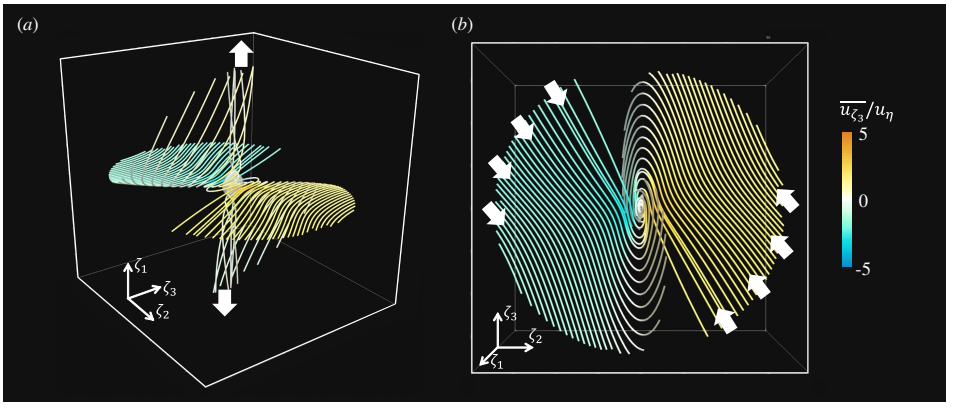

Figure 10: Mean streamlines around the shear layer for the Newtonian case: (a) diagonal view; (b) top view from the ζ_1 direction. The isosurface of $\overline{I_S}/\tau_\eta^{-1} = 1.1$ (white) visualises the shear layer. The streamlines that passes the line connecting $(\zeta_1/\eta, \zeta_2/\eta, \zeta_3/\eta) = (-5, 60, 30)$ and $(5, -60, -30)$ are visualised in a spherical domain with a radius of 80η. The arrows indicate the flow direction.

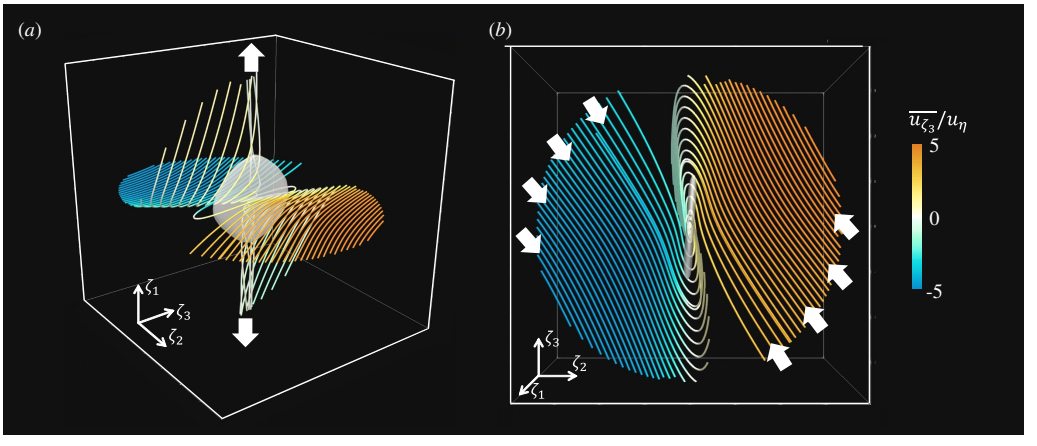

Figure 11: The same as figure 10 but for $Wi = 4.6$.

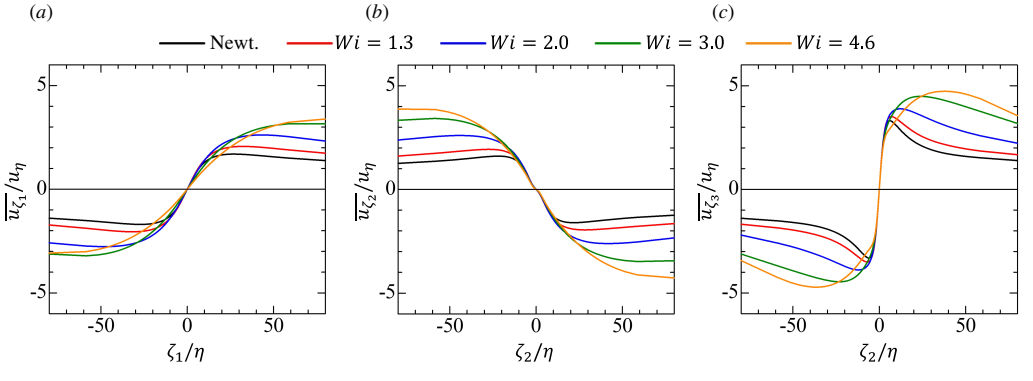

Figure 12: Mean velocity profiles across the shear layer. (a) $\overline{u_{\zeta_1}}$ on the ζ_1 axis, (b) $\overline{u_{\zeta_2}}$ on the ζ_2 axis and (c) $\overline{u_{\zeta_3}}$ on the ζ_2 axis. The profiles are shown along the lines that pass the centre of the shear layer, $(\zeta_1, \zeta_2, \zeta_3) = (0, 0, 0)$.

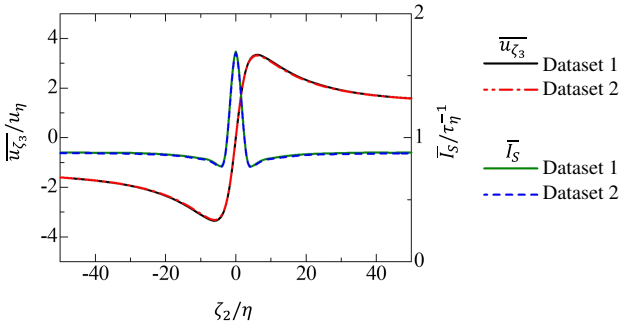

Figure 13: The mean velocity and shear intensity profiles across the shear layer obtained from two distinct datasets, each representing one half of the computational domain (Newtonian case). Their differences provide a measure of statistical errors.

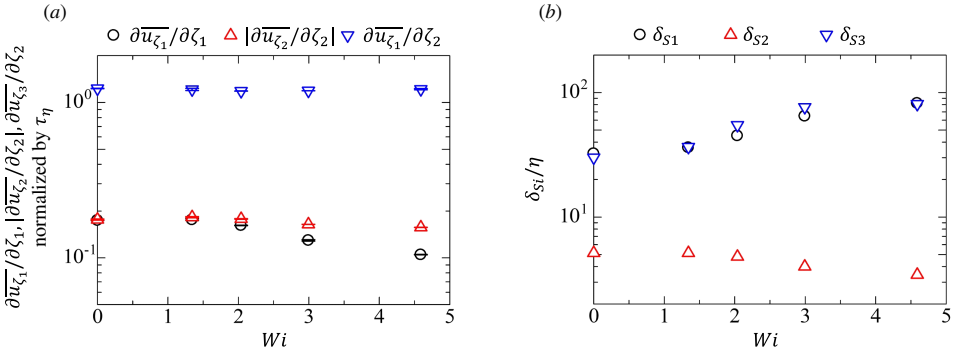

Figure 14: The Weissenberg number (Wi) dependence of (a) the mean velocity gradients associated with shear and strain in the shear layer, $\partial\overline{u_{\zeta_1}}/\partial\zeta_1$, $|\partial\overline{u_{\zeta_2}}/\partial\zeta_2|$ and $\partial\overline{u_{\zeta_3}}/\partial\zeta_2$ and (b) the length scales of the shear layer in the ζ_1, ζ_2 and ζ_3 directions, which are denoted by δ_{S1}, δ_{S2} and δ_{S3}, respectively. The Kolmogorov length (η) and time (τ_η) scales are used for normalisation. The maximum values of the mean velocity gradients near the shear layers are plotted in (a), where $|\overline{u_{\zeta_2}}/\zeta_2|$ is shown instead of $\partial\overline{u_{\zeta_2}}/\partial\zeta_2$ for the usage of the logarithmic scale. In (a), the error bars represent the statistical errors estimated with the two datasets, generated by dividing the computational domain into two equal halves.

profiles reveals minimal differences in their distributions, demonstrating a high degree of statitsical convergence. It indicates that even with half the number of statistical samples for the shear layers, the results remain consistent. Therefore, the conclusions drawn from the statistical analysis of the shear layer are robust and not skewed by statistical errors.

The velocity jumps of shear layers are further examined by plotting the maximum values of the mean velocity gradients against Wi in figure 14(a). The error bars indicate the statistical errors by illustrating the values obtained from two separate datasets. Both datasets yield almost identical values for the mean velocity gradients, and the statistical errors are negligible. As shown in figure 12, $\partial\overline{u_{\zeta_1}}/\partial\zeta_1$ and $\partial\overline{u_{\zeta_3}}/\partial\zeta_2$ become the largest at $\zeta_1 = 0$ and $\zeta_2 = 0$ while $\partial\overline{u_{\zeta_2}}/\partial\zeta_2$ has negative peaks. The mean velocity gradient related to shearing motion, $\partial\overline{u_{\zeta_3}}/\partial\zeta_2$, normalised by the Kolmogorov time scale is similar for Newtonian and viscoelastic cases and hardly varies with Wi. The extensive strain, $\partial\overline{u_{\zeta_1}}/\partial\zeta_1$, becomes weak as Wi increases. Similarly, the compressible strain, $\partial\overline{u_{\zeta_2}}/\partial\zeta_2$, becomes weak with increasing Wi although the decrease in $|\partial\overline{u_{\zeta_2}}/\partial\zeta_2|$ with Wi is not as significant as that in $\partial\overline{u_{\zeta_1}}/\partial\zeta_1$ for high Wi.

The constant values of $\partial\overline{u_{\zeta_3}}/\partial\zeta_2$ within the shear layer are observed when normalised by the Kolmogorov time scale, which is defined based on the solvent dissipation rate of kinetic energy. In Newtonian turbulence, the dissipation of kinetic energy is predominantly driven by shearing motion, specifically related to $\partial u_{\zeta_3}/\partial\zeta_2$ in the shear layers (Nagata *et al.* 2020; Das & Girimaji 2020). Mathematically, irrotational strain without shear, represented by $\nabla \boldsymbol{u}_E$ in the triple decomposition, can also contribute to dissipation. However, it has been demonstrated that this type of motion does not significantly contribute to dissipation as compared to shearing motion in Newtonian turbulence (Nagata *et al.* 2020; Das & Girimaji 2020). Consequently, $\partial\overline{u_{\zeta_3}}/\partial\zeta_2$ normalised by the Kolmogorov time scale tends to remain constant across different Reynolds number flows (Watanabe *et al.* 2020). The present results indicate that in viscoelastic cases, the physical mechanism underlying the constancy of normalised $\partial\overline{u_{\zeta_3}}/\partial\zeta_2$ for different Wi values is the predominance of shearing motion in the dissipation by the solvent. Below, the Wi dependence of the mean solvent dissipation in turbulence is well explained by changes in dissipation due to shear layers, further confirming that shear layer structures are responsible for solvent dissipation even in viscoelastic turbulence. On the other hand, $\partial\overline{u_{\zeta_1}}/\partial\zeta_1$ and $|\partial\overline{u_{\zeta_2}}/\partial\zeta_2|$ show a clear dependence on Wi even when normalised by the Kolmogorov time scale. These components are associated with the straining flow around shear layers. In Newtonian turbulence, the configuration analysis of vortex tubes and shear layers has suggested that the straining flow acting on shear layers is partially induced by nearby vortex tubes (Watanabe & Nagata 2022). Therefore, the observed suppression of vortex formations from shear layers in viscoelastic turbulence, as discussed in figures 10 and 11, is likely related to the weakened straining flow observed as the decreases in $\partial\overline{u_{\zeta_1}}/\partial\zeta_1$ and $|\partial\overline{u_{\zeta_2}}/\partial\zeta_2|$ at higher Wi values. Consistently, the weakened irrotational strain is further confirmed by the Wi dependency of I_E in figure 5(c).

The Wi dependence of $\partial\overline{u_{\zeta_1}}/\partial\zeta_1$ and $\partial\overline{u_{\zeta_3}}/\partial\zeta_2$ has an important implication for vorticity dynamics. The interaction between the shear and biaxial strain causes large enstrophy production (Watanabe *et al.* 2020; Hayashi *et al.* 2021a). This is explained by the vorticity arising from large $\partial\overline{u_{\zeta_3}}/\partial\zeta_2$ of shearing motion, which is stretched by the extensive strain in the ζ_1 direction with large $\partial\overline{u_{\zeta_1}}/\partial\zeta_1$. The vorticity due to shear is unlikely to be influenced by viscoelasticity, as attested by the weak Wi dependence of $\partial\overline{u_{\zeta_3}}/\partial\zeta_2$, whereas the extensive strain $\partial\overline{u_{\zeta_1}}/\partial\zeta_1$ becomes weaker with increasing Wi. Therefore, the enstrophy production due to shear and surrounding straining motion is weakened as the viscoelastic effects become significant. This is also confirmed below with the enstrophy budget near the shear layer.

Another interesting behaviour is in the balance between $\partial\overline{u_{\zeta_1}}/\partial\zeta_1$ and $\partial\overline{u_{\zeta_2}}/\partial\zeta_2$. The incompressible condition imposes $\partial u_{\zeta_1}/\partial\zeta_1 + \partial u_{\zeta_2}/\partial\zeta_2 + \partial u_{\zeta_3}/\partial\zeta_3 = 0$. In the Newtonian case, $\partial\overline{u_{\zeta_1}}/\partial\zeta_1 + \partial\overline{u_{\zeta_2}}/\partial\zeta_2 \approx 0$ is satisfied in the shear layer, suggesting that the two-dimensional strain is acting on the shear layer with approximately equal strength of the extension and compression. However, the extensive strain $\partial\overline{u_{\zeta_1}}/\partial\zeta_1$ becomes weaker than the compressive strain $\partial\overline{u_{\zeta_2}}/\partial\zeta_2$ at high Wi. This can cause an additional extensive strain $\partial\overline{u_{\zeta_3}}/\partial\zeta_3 > 0$ in the shear-flow direction. The magnitude of the mean velocity vectors in figures 7–9 is expressed with the length of the arrows. In the Newtonian case, the mean velocity in the ζ_3 direction is negligibly small within the shear layer, which is along the ζ_3 axis at $\zeta_2 = 0$ in figure 7(a). However, in figure 9(a) with $Wi = 4.6$, the mean velocities with $\overline{u_{\zeta_3}} > 0$ and $\overline{u_{\zeta_3}} < 0$ are observed for $\zeta_3 > 0$ and $\zeta_3 < 0$ in the shear layer, respectively, confirming that the extensive strain is indeed acting in the ζ_3 direction. As discussed below, this Wi dependence of $\overline{u_{\zeta_3}}$ is important for the polymer stress within the shear layers.

Figure 14(b) shows the Wi dependence of the size of the shear layers in the three directions evaluated with the mean shear intensity $\overline{I_S}$. Here, a normalised mean shear intensity $\hat{I}_S$ is defined as $\hat{I}_S(\zeta_1,\zeta_2,\zeta_3) = [\overline{I_S}(\zeta_1,\zeta_2,\zeta_3) - \langle I_S\rangle]/[\overline{I_S}(0,0,0) - \langle I_S\rangle]$. Because of $\overline{I_S} = \langle I_S\rangle$ at

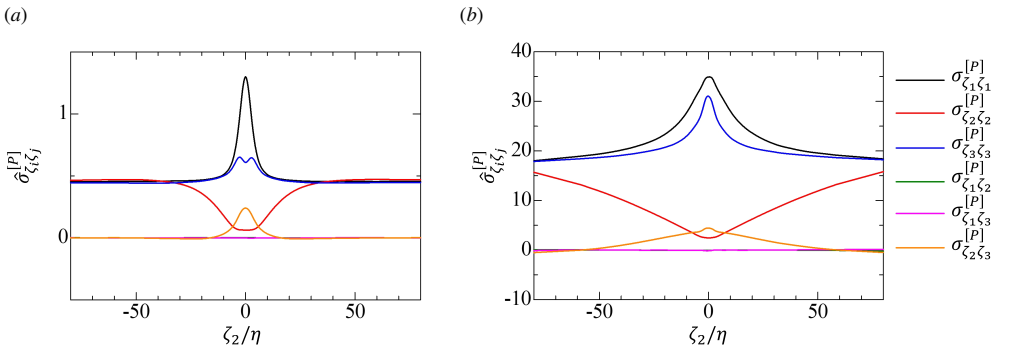

Figure 15: Mean polymer stresses $\sigma^{[P]}_{\zeta_i\zeta_j}$ near the shear layer for (*a*) $Wi = 1.3$ and (*b*) $Wi = 4.6$. The results are shown for the non-dimensionalised stresses $\hat{\sigma}^{[P]}_{\zeta_i\zeta_j} = \overline{\sigma^{[P]}_{\zeta_i\zeta_j}}/(\rho u_\eta^2)$ and are plotted against ζ_2/η at $(\zeta_1, \zeta_3) = (0, 0)$. The stress tensor is evaluated in the shear coordinate $(\zeta_1, \zeta_2, \zeta_3)$.

large $|\zeta_i|$, $\hat{I}_S$ is equal to 1 at the shear layer centre and decreases to 0 as $|\zeta_i|$ increases. The length scale of the shear layer in the ζ_1 direction, δ_{S1}, is quantified as the distance between two points of $\hat{I}_S(\zeta_1, 0, 0) = 0.1$ on the ζ_1 axis at $(\zeta_2, \zeta_3) = (0, 0)$. Similarly, the length scales in the ζ_2 and ζ_3 directions, δ_{S2} and δ_{S3}, are quantified with the locations of $\hat{I}_S(0, \zeta_2, 0) = 0.1$ and $\hat{I}_S(0, 0, \zeta_3) = 0.1$, respectively. In figure 14(*b*), δ_{S1} and δ_{S3} increase and δ_{S2} decreases as Wi becomes large. Thus, the shear layers become larger in the layer-parallel directions and thinner in the normal direction as the viscoelastic effects become more important. This geometrical change also agrees with the visualised shear layers in figure 2. The shear layer is one of the smallest-scale vortical structures, manifesting with a sheet-like geometry. In Newtonian turbulence, the thickness of these shear layers scales with η (Watanabe *et al.* 2020; Fiscaletti *et al.* 2021; Hayashi *et al.* 2021*a*). However, as Wi increases, the thickness of these layers, when normalised by η, decreases. This observation indicates that the Kolmogorov scale does not adequately characterise the length scale of vortical structures at the smallest scales in viscoelastic turbulence.

The above viscoelastic effects on the mean properties of the shear layers are significant at high Wi. However, the shear layers in viscoelastic turbulence at low Wi behave similarly to Newtonian turbulence. In figure 14(*a*), the mean velocity gradients of the biaxial strain hardly change due to the viscoelastic effects up to $Wi \approx 2$ whereas the gradient in the ζ_1 direction begins to decrease for $Wi > 2$. Similarly, the shear layer thickness δ_{S2} is influenced by viscoelasticity for $Wi > 2$. These results imply that the shear layers in viscoelastic turbulence are similar to those in Newtonian turbulence until Wi becomes sufficiently large. Once Wi exceeds a certain criterion about $Wi \approx 2$, viscoelasticity drastically influences the shear layers, as also observed as the changes in the kinetic energy spectra (Ferreira *et al.* 2016).

4.3. *Polymer stress distribution near the shear layers*

The velocity gradients due to the shear and strain are expected to affect the polymer molecules near the shear layers. The present study examines the polymer stress tensor expressed in the shear coordinate, $\sigma^{[P]}_{\zeta_i\zeta_j}$, whose averages taken around the shear layer are $\overline{\sigma^{[P]}_{\zeta_i\zeta_j}}$. Here, the normalised mean stresses are defined as $\hat{\sigma}^{[P]}_{\zeta_i\zeta_j} = \overline{\sigma^{[P]}_{\zeta_i\zeta_j}}/(\rho u_\eta^2)$. Figure 15 shows six independent components of the mean polymer stress tensor for $Wi = 1.3$ and 4.6 across the shear layer. The mean polymer stresses vary significantly near the shear layer, suggesting that

the shear layers impact the extension of the polymer molecules. Here, spatial variations near the shear layer are observed for $\hat{\sigma}^{[P]}_{\zeta_1\zeta_1}$, $\hat{\sigma}^{[P]}_{\zeta_2\zeta_2}$, $\hat{\sigma}^{[P]}_{\zeta_3\zeta_3}$ and $\hat{\sigma}^{[P]}_{\zeta_2\zeta_3}$, which are strongly influenced by the shear layers, whereas the remaining components are almost zero. The polymer stress tensor is defined with the conformation tensor evolving according to (2.8), which is helpful to understand the relation between the conformation tensor in the shear coordinate, $C_{\zeta_i\zeta_j}$, and the velocity jumps around shear layers. The extensive strain with $\partial\overline{u_{\zeta_1}}/\partial\zeta_1 > 0$ and compressive strain with $\partial\overline{u_{\zeta_2}}/\partial\zeta_2 < 0$ appear in the governing equations of $C_{\zeta_1\zeta_1}$ and $C_{\zeta_2\zeta_2}$ as $C_{\zeta_1\zeta_1}(\partial u_{\zeta_1}/\partial\zeta_1)$ and $C_{\zeta_2\zeta_2}(\partial u_{\zeta_2}/\partial\zeta_2)$, respectively. For $C_{\zeta_1\zeta_1}$, the extensive strain causes stretching of the polymer molecules, which results in large $C_{\zeta_1\zeta_1}$. For the same reason, the compressive strain decreases $C_{\zeta_2\zeta_2}$. These contributions of the straining flow to $C_{\zeta_1\zeta_1}$ and $C_{\zeta_2\zeta_2}$ explain large $\hat{\sigma}^{[P]}_{\zeta_1\zeta_1}$ and small $\hat{\sigma}^{[P]}_{\zeta_2\zeta_2}$ within the shear layers. Similarly, $\partial\overline{u_{\zeta_3}}/\partial\zeta_2 > 0$ due to the shear causes the polymer distortion and contributes to an increase of $C_{\zeta_2\zeta_3} = C_{\zeta_3\zeta_2}$. For $C_{\zeta_2\zeta_3}$, the compressive strain in the ζ_2 direction may contribute to a reduction of $C_{\zeta_2\zeta_3}$. However, figure 14(a) has shown that the shear causes a larger velocity gradient than the strain, namely $\partial u_{\zeta_3}/\partial\zeta_2 > |\partial u_{\zeta_2}/\partial\zeta_2|$. Therefore, an increase of $C_{\zeta_2\zeta_3}$ due to the shear can surpass a decrease due to the compressive strain. Thus, $C_{\zeta_2\zeta_3}$, namely $\hat{\sigma}^{[P]}_{\zeta_2\zeta_3}$, is locally large near the shear layer. A comparison between $Wi = 1.3$ and 4.6 suggests that the relative importance of $\hat{\sigma}^{[P]}_{\zeta_3\zeta_3}$ compared to the other components depends on Wi: $\hat{\sigma}^{[P]}_{\zeta_3\zeta_3}$ within the shear layer ($\zeta_2 \approx 0$) is as large as $\hat{\sigma}^{[P]}_{\zeta_1\zeta_1}$ at $Wi = 4.6$ whereas $\hat{\sigma}^{[P]}_{\zeta_3\zeta_3}$ is much smaller than $\hat{\sigma}^{[P]}_{\zeta_1\zeta_1}$ for $Wi = 1.3$. This Wi dependence is explained by $\partial\overline{u_{\zeta_3}}/\partial\zeta_3$, which increases from zero as Wi increases because of the imbalance between the extension and compression of the straining flow in figure 14(a). For $Wi > 2$, the extensive strain in the ζ_3 direction with $\partial\overline{u_{\zeta_3}}/\partial\zeta_3 > 0$ begins to act in the shear layer. This strain causes an increase of $C_{\zeta_3\zeta_3}$ due to the polymer stretching, $C_{\zeta_3\zeta_3}(\partial u_{\zeta_3}/\partial\zeta_3) > 0$, which appears in the governing equation for $C_{\zeta_3\zeta_3}$. This additional extensive strain becomes important only for sufficiently high Wi. Therefore, the large peak of $\hat{\sigma}^{[P]}_{\zeta_3\zeta_3}$ within the shear layer is observed at $Wi = 4.6$ but not at $Wi = 1.3$.

Figures 16 and 17 visualise the two-dimensional profiles of $\hat{\sigma}^{[P]}_{\zeta_i\zeta_j}$ on the ζ_2–ζ_3 plane at $\zeta_1 = 0$ for $Wi = 1.3$ and 3.0. White lines are the isolines of $\overline{I_S}$, which mark the location of the shear layer. Qualitative differences between the large and small Wi cases are observed for $\hat{\sigma}^{[P]}_{\zeta_3\zeta_3}$ and $\hat{\sigma}^{[P]}_{\zeta_2\zeta_3}$. The difference in $\hat{\sigma}^{[P]}_{\zeta_3\zeta_3}$ is due to the stretching in the ζ_3 direction arising from the imbalance in the strain, as discussed above. As a result, $\hat{\sigma}^{[P]}_{\zeta_3\zeta_3}$ for $Wi = 3.0$ becomes large within the shear layer. However, large $\hat{\sigma}^{[P]}_{\zeta_3\zeta_3}$ appears on the sides of the shear layer for $Wi = 1.3$. A similar difference is found for $\hat{\sigma}^{[P]}_{\zeta_2\zeta_3}$, which is large within the shear layer at $Wi = 3.0$. Especially, very large $\hat{\sigma}^{[P]}_{\zeta_2\zeta_3}$ appears along the ζ_3 axis at $\zeta_2 = 0$ above and below the centre of the shear layer. The governing equation of $C_{\zeta_2\zeta_3}$ contains $C_{\zeta_2\zeta_3}(\partial\overline{u_{\zeta_3}}/\partial\zeta_3)$, which causes an increase of $C_{\zeta_2\zeta_3}$ at high Wi because of the Wi dependence of $\partial\overline{u_{\zeta_3}}/\partial\zeta_3$ explained above. As discussed below, the Wi dependence of $\sigma^{[P]}_{\zeta_3\zeta_3}$ is crucial in the vorticity dynamics of shear layers.

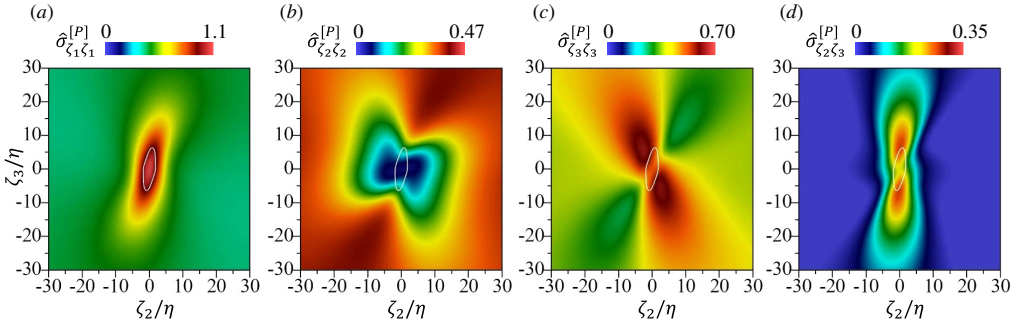

Figure 16: Non-dimensionalised mean polymer stresses $\hat{\sigma}^{[P]}_{\zeta_i\zeta_j}$ near the shear layer on the ζ_2–ζ_3 plane at $\zeta_1 = 0$ for $Wi = 1.3$. (*a*) $\hat{\sigma}^{[P]}_{\zeta_1\zeta_1}$, (*b*) $\hat{\sigma}^{[P]}_{\zeta_2\zeta_2}$, (*c*) $\hat{\sigma}^{[P]}_{\zeta_3\zeta_3}$ and (*d*) $\hat{\sigma}^{[P]}_{\zeta_2\zeta_3}$.

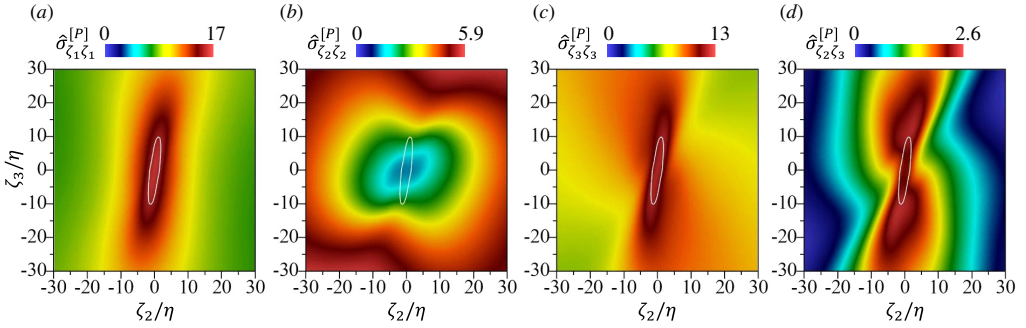

Figure 17: The same as figure 16 but for $Wi = 3.0$.

4.4. *The relevance of shear layers to vorticity dynamics and kinetic energy dissipation*

The transport equation of enstrophy for viscoelastic turbulence is written as

$$\frac{D\omega^2/2}{Dt} = \underbrace{\omega_i S_{ij}\omega_j}_{P_\omega} + \underbrace{\nu^{[S]}\frac{\partial^2\omega^2/2}{\partial x_j\partial x_j}}_{D_\omega} - \underbrace{\nu^{[S]}\frac{\partial\omega_i}{\partial x_j}\frac{\partial\omega_i}{\partial x_j}}_{\varepsilon_\omega} + \underbrace{\omega_i\epsilon_{nji}\frac{\partial^2\sigma^{[P]}_{mj}}{\partial x_m\partial x_n}}_{V_\omega}, \tag{4.1}$$

where P_ω is the production term, D_ω is the viscous diffusion term, ε_ω is the viscous dissipation term and V_ω represents an enstrophy change due to the interaction between vorticity and polymer stresses. The last term is absent in Newtonian fluids. The average of $D\omega^2/2/Dt$, $\langle D\omega^2/2/Dt\rangle$, is zero in HIT because the statistical stationarity and homogeneity assume $\langle\partial f/\partial t\rangle = 0$ and $\langle\partial f/\partial x_i\rangle = 0$ for any variable f. However, when the average of $D(\omega^2/2)/Dt$ is conditionally taken for certain regions in HIT, such as shear layers or vortex tubes, the conditional average of $D(\omega^2/2)/Dt$ is not necessarily zero because the enstrophy amplification or attenuation may occur in a specific region in HIT.

Figure 18(*a*) shows the enstrophy budget across the shear layer in Newtonian turbulence, with the conditional averages of each term plotted against ζ_2/η at $(\zeta_1, \zeta_3) = (0, 0)$. The enstrophy production P_ω becomes large within the shear layer because of the stretching of vorticity arising from the shear by the extensive strain in the ζ_1 direction. The enstrophy is locally large within the shear layer. Therefore, the diffusion term D_ω reduces and increases the enstrophy inside and outside the shear layer, respectively, transferring the enstrophy from the shear layer to the outside. The dissipation ε_ω is also large near the shear layer and has

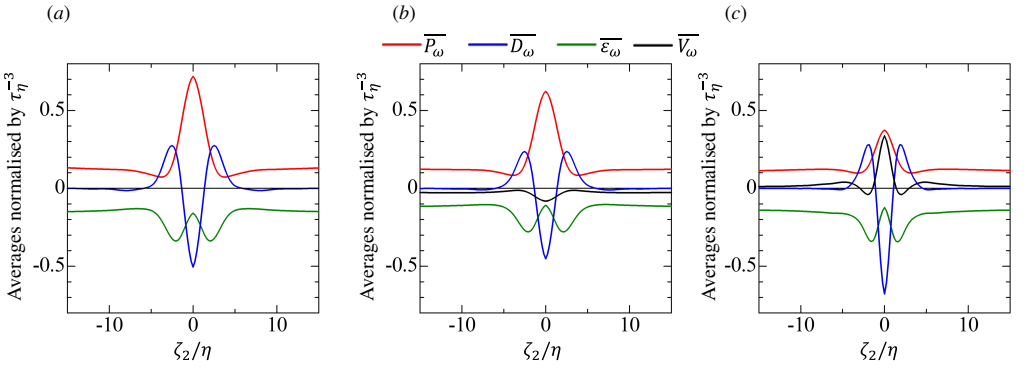

Figure 18: The enstrophy budget near the shear layer for (a) Newtonian case, (b) $Wi = 1.3$ and (c) $Wi = 3.0$. The averages of (4.1), $\overline{P_\omega}$, $\overline{D_\omega}$, $\overline{\varepsilon_\omega}$ and $\overline{V_\omega}$, normalised by the Kolmogorov time scale τ_η are plotted against ζ_2/η at $(\zeta_1, \zeta_3) = (0, 0)$.

negative peaks at the locations where the enstrophy growth due to the viscous diffusion occurs. These results of the enstrophy budget in HIT are consistent with those in a turbulent planar jet (Hayashi *et al.* 2021*b*).

Figures 18(b, c) present the enstrophy budget in viscoelastic cases. The negative peak of the diffusion term D_ω at $\zeta_2 = 0$ at $Wi = 3.0$ is larger than in the Newtonian case. The diffusion is related to the enstrophy gradient on both sides of the shear layer. Because the shear layer thickness decreases with Wi, the local enstrophy gradient in the ζ_2 direction also becomes large, resulting in the large negative peak of $\overline{D_\omega}$ in the shear layer. On the other hand, the peak of the production term P_ω decreases as Wi increases from the Newtonian case. Large P_ω within the shear layer is attributed to shear $\partial u_{\zeta_3}/\partial\zeta_2$ and extensive strain $\partial u_{\zeta_1}/\partial\zeta_1$. The shear contributes to the vorticity vector in the ζ_1 direction, ω_{ζ_1}. Production P_ω has a term of $\omega_{\zeta_1} S_{\zeta_1\zeta_1} \omega_{\zeta_1}$, to which the shear and extensive strain contribute in the form of $(\partial u_{\zeta_3}/\partial\zeta_2)^2(\partial u_{\zeta_1}/\partial\zeta_1)$. Thus, the large velocity gradients, $\partial u_{\zeta_3}/\partial\zeta_2$ and $\partial u_{\zeta_1}/\partial\zeta_1$, of the shear layer cause the large enstrophy production. Figure 14(a) has already shown that as Wi increases, the extensive strain $\partial u_{\zeta_1}/\partial\zeta_1$ becomes weak, especially when Wi exceeds about 2. For this reason, the enstrophy production becomes small at high Wi. In addition to this change in the enstrophy production, the vorticity/polymer interaction term V_ω changes its role in the vorticity dynamics within the shear layer. At $Wi = 1.3$, $\overline{V_\omega}$ is negative in the shear layer and acts as a destruction term of enstrophy. However, it has a large positive peak comparable to P_ω at $Wi = 3.0$ and acts as an additional production term. This transition implies that shearing motion changes from an inertia-dominated state to an inertio-elasticity dominated state. These observations are consistent with those reported by Abreu *et al.* (2022), where a similar transition from a sink to a source role for the term V_ω was noted with increasing values of Wi, even though their analysis was not exclusively focused on shear layers. In wall-bounded turbulent shear flows, the interaction between vorticity and polymers introduces a sink term for the streamwise component of enstrophy, leading to a reduction in streamwise vorticity (Kim *et al.* 2007). Conversely, when considering enstrophy defined for the mean velocity, namely the squared mean vorticity, this interaction acts as a source term for its streamwise component near the wall (Song *et al.* 2021).

The Wi dependence of the production and destruction of enstrophy due to the polymers, V_ω, is examined by considering the following decomposition based on the vorticity vector in

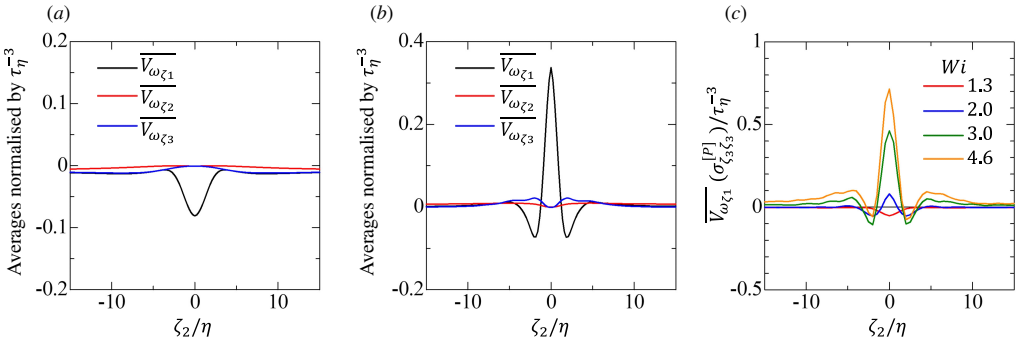

Figure 19: The mean profiles of decomposed vorticity/polymer interaction terms, (4.2), in the enstrophy transport equation across the shear layer for (*a*) $Wi = 1.3$ and (*b*) $Wi = 3.0$. (*c*) The mean profile of a component of the interaction between ω_{ζ_1} and $\sigma^{[P]}_{\zeta_3\zeta_3}$, the third term $\overline{V_{\omega_{\zeta 1}}}(\sigma^{[P]}_{\zeta_3\zeta_3})$ in (4.3), across the shear layer. The results taken at $(\zeta_1, \zeta_3) = (0, 0)$ are plotted against ζ_2/η.

the shear coordinate:

$$V_\omega = \underbrace{\omega_{\zeta_1}\epsilon_{\zeta_n\zeta_j\zeta_1}\frac{\partial^2\sigma^{[P]}_{\zeta_m\zeta_j}}{\partial x_{\zeta_m}\partial x_{\zeta_n}}}_{V_{\omega_{\zeta 1}}} + \underbrace{\omega_{\zeta_2}\epsilon_{\zeta_n\zeta_j\zeta_2}\frac{\partial^2\sigma^{[P]}_{\zeta_m\zeta_j}}{\partial x_{\zeta_m}\partial x_{\zeta_n}}}_{V_{\omega_{\zeta 2}}} + \underbrace{\omega_{\zeta_3}\epsilon_{\zeta_n\zeta_j\zeta_3}\frac{\partial^2\sigma^{[P]}_{\zeta_m\zeta_j}}{\partial x_{\zeta_m}\partial x_{\zeta_n}}}_{V_{\omega_{\zeta 3}}}, \tag{4.2}$$

which represents the interaction of the vorticity in the ζ_i direction with the polymer stresses. Figures 19(*a*, *b*) show the averages of these decomposed terms for $Wi = 1.3$ and 3.0. The ζ_1-vorticity component has a dominant contribution to this term, whereas the averages of the other terms are negligibly small. Thus, the polymer-stress interaction with the ζ_1-vorticity, that is, a vorticity due to shear, destroys and produces enstrophy for $Wi = 1.3$ and 3.0, respectively.

To further examine the Wi-dependece of V_ω, $V_{\omega_{\zeta 1}}$ is decomposed into six terms with different components of the polymer stress tensor as

$$\begin{aligned} V_{\omega_{\zeta 1}} = {} & \omega_{\zeta_1}\frac{\partial^2\sigma^{[P]}_{\zeta_1\zeta_3}}{\partial x_{\zeta_1}\partial x_{\zeta_2}} + \omega_{\zeta_1}\frac{\partial^2\sigma^{[P]}_{\zeta_2\zeta_3}}{\partial x_{\zeta_2}\partial x_{\zeta_2}} + \omega_{\zeta_1}\frac{\partial^2\sigma^{[P]}_{\zeta_3\zeta_3}}{\partial x_{\zeta_3}\partial x_{\zeta_2}} \\ & - \omega_{\zeta_1}\frac{\partial^2\sigma^{[P]}_{\zeta_1\zeta_2}}{\partial x_{\zeta_1}\partial x_{\zeta_3}} - \omega_{\zeta_1}\frac{\partial^2\sigma^{[P]}_{\zeta_2\zeta_2}}{\partial x_{\zeta_2}\partial x_{\zeta_3}} - \omega_{\zeta_1}\frac{\partial^2\sigma^{[P]}_{\zeta_3\zeta_2}}{\partial x_{\zeta_3}\partial x_{\zeta_3}}. \end{aligned} \tag{4.3}$$

The distributions of the stresses near the shear layer in figure 15 suggest that the terms with $\sigma^{[P]}_{\zeta_2\zeta_2}$, $\sigma^{[P]}_{\zeta_3\zeta_3}$ and $\sigma^{[P]}_{\zeta_3\zeta_2}$ have dominant contributions to $V_{\omega_{\zeta 1}}$. We have examined all the decomposed terms near the shear layer for all simulations with different Wi and noticed that the third term with $\sigma^{[P]}_{\zeta_3\zeta_3}$, denoted by $V_{\omega_{\zeta 1}}(\sigma^{[P]}_{\zeta_3\zeta_3})$, is responsible for the Wi dependence of V_ω observed in figure 18. Figure 19(*c*) presents the mean profile of $V_{\omega_{\zeta 1}}(\sigma^{[P]}_{\zeta_3\zeta_3})$ across the shear layer. For small Wi, this term is small even within the shear layer. However, a large positive peak appears for $Wi = 3.0$ and 4.6. Because of this Wi dependence of the interaction between the vorticity in the ζ_1 direction with the normal polymer stress in the ζ_3 direction, the role of V_ω changes with Wi. The shear expressed as $\partial u_{\zeta_3}/\partial\zeta_2 > 0$ contributes to large positive ω_{ζ_1}. Therefore, the sign of $V_{\omega_{\zeta 1}}(\sigma^{[P]}_{\zeta_3\zeta_3})$ depends on $\partial^2\sigma^{[P]}_{\zeta_3\zeta_3}/\partial x_{\zeta_3}\partial x_{\zeta_2}$. The

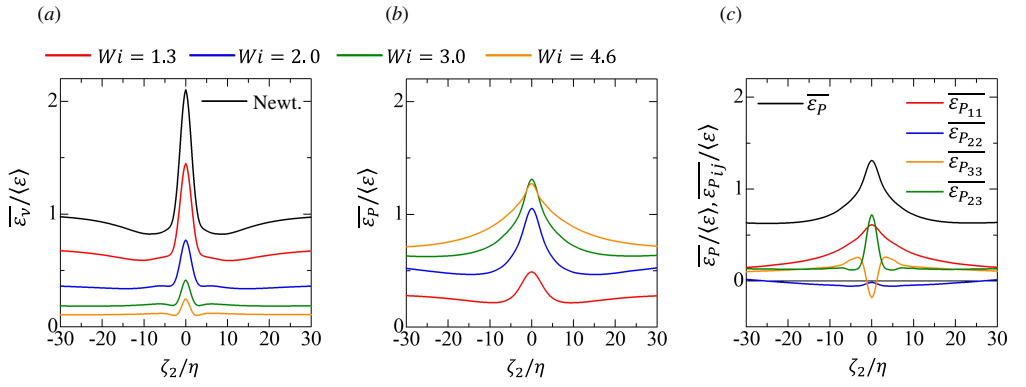

Figure 20: The mean kinetic energy dissipation rates due to (a) viscous stress, $\overline{\varepsilon_\nu}$, and (b) polmer stress, $\overline{\varepsilon_P}$, near the shear layer. (c) Contributions of different polymer-stress components to the dissipation rate, (4.4), at $Wi = 3.0$. The dissipation rates are normalised by the volume-averaged total dissipation rate $\langle\varepsilon\rangle = \langle\varepsilon_\nu + \varepsilon_P\rangle$. The results taken at $(\zeta_1, \zeta_3) = (0, 0)$ are plotted against ζ_2/η.

distributions of $\sigma^{[P]}_{\zeta_3\zeta_3}$ for low and high Wi have been presented in figures 16(c) and 17(c), respectively. For high Wi, large $\overline{\sigma^{[P]}_{\zeta_3\zeta_3}}$ distributes from the first to third quadrants along the shear layer, which is slightly tilted from the ζ_3 direction. Therefore, an instantaneous profile of $\sigma^{[P]}_{\zeta_3\zeta_3}$ often has a positive peak in the first or third quadrant, which can cause positive $\partial^2\sigma^{[P]}_{\zeta_3\zeta_3}/\partial x_{\zeta_3}\partial x_{\zeta_2}$ at $(\zeta_2, \zeta_3) = (0, 0)$, namely the viscoelastic enstrophy production at high Wi. On the other hand, large $\overline{\sigma^{[P]}_{\zeta_3\zeta_3}}$ at low Wi appears in the second and third quadrants, resulting in negative $\partial^2\sigma^{[P]}_{\zeta_3\zeta_3}/\partial x_{\zeta_3}\partial x_{\zeta_2}$ with the enstrophy destruction. As discussed above, these differences related to $\sigma^{[P]}_{\zeta_3\zeta_3}$ are attributed to the viscoelastic effects on the mean flow field around the shear layer, which significantly changes once Wi exceeds about 2.

In viscoelastic turbulence, kinetic energy dissipation rates due to viscous and polymer stresses are written as $\varepsilon_\nu = 2\nu S_{ij}S_{ij}$ and $\varepsilon_P = S_{ij}\sigma^{[P]}_{ij}$, respectively. Figures 20$(a,\ b)$ show the profiles of the mean dissipation rates, $\overline{\varepsilon_\nu}$ and $\overline{\varepsilon_P}$, near the shear layer, which are normalised by the volume-averaged total dissipation rate $\langle\varepsilon\rangle = \langle\varepsilon_\nu + \varepsilon_P\rangle$. Both dissipation rates have peaks at the centre of the shear layer. The viscous and polymer dissipation rates tend to decrease and increase, respectively, as Wi increases. As a result, the polymer stress contributes more to kinetic energy dissipation than the viscous stress for $Wi \geqslant 2.0$.

The dissipation rate due to the polymer can be decomposed into the contributions from each component of the polymer stress tensor in the shear coordinate as

$$\varepsilon_P = \sum_{\alpha=1}^{3}\sum_{\beta=1}^{3}\varepsilon_{P_{\alpha\beta}} \quad \text{with} \quad \varepsilon_{P_{\alpha\beta}} = S_{\zeta_\alpha\zeta_\beta}\sigma^{[P]}_{\zeta_\alpha\zeta_\beta}, \tag{4.4}$$

where the summation is not applied to the Greek indices. The mean profiles of velocity and polymer stress around the shear layer indicate that $\varepsilon_{P_{11}}$, $\varepsilon_{P_{22}}$, $\varepsilon_{P_{33}}$ and $\varepsilon_{P_{23}}$ are dominant because of the large velocity gradients and significant variations of the polymer stresses within the shear layer. Figure 20(c) shows the mean profiles of these dissipation components near the shear layer for $Wi = 3.0$. The large dissipation rate by the polymer within the shear layer is caused by $\varepsilon_{P_{11}}$ and $\varepsilon_{P_{23}}$. These components become large because of the extensive

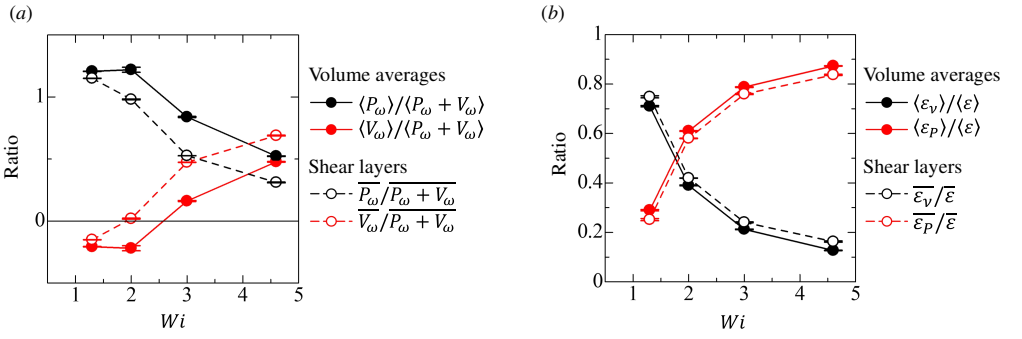

Figure 21: (a) The Weissenberg number (Wi) dependence of averages of the production term P_ω and vorticity/polymer interaction term V_ω in the enstrophy transport equation (4.1). The averages are calculated with the conventional volume averages, $\langle P_\omega \rangle$ and $\langle V_\omega \rangle$, or the conditional averages, $\overline{P_\omega}$ and $\overline{V_\omega}$, at the centre of the shear layer $(\zeta_1, \zeta_2, \zeta_3) = (0, 0, 0)$. The sum of the two terms normalises each average. (b) The Wi dependence of averages of the viscous dissipation rate ε_ν and polymer dissipation rate ε_P, which are calculated with the volume averages or conditional averages at the centre of the shear layer. Each average is normalised by the average of the total dissipation $\varepsilon = \varepsilon_\nu + \varepsilon_P$. The error bars represent the statistical errors estimated with the two datasets, generated by dividing the computational domain into two equal halves.

strain and shear, which also contribute to the amplification of the corresponding components of the polymer stress tensor.

For the present case, $\overline{\varepsilon_P}$ is always positive even at large ζ_2, where $\overline{\varepsilon_P}$ asymptotically approaches the volume average of ε_P. Thus, the polymer stress leads to the dissipation of the turbulent kinetic energy. The large positive $\varepsilon_{P_{11}}$ in figure 20(c) is attributed to the three-dimensional flow around the shear layers, specifically an extensional strain in the normal direction of the shear plane (ζ_2–ζ_3 plane). In DNS of viscoelastic planar jets, an opposite energy conversion to turbulent kinetic energy was observed in the potential core region, where the flow is characterised by a two-dimensional mean shear (Guimarães *et al.* 2023). These studies suggest that the three-dimensionality of small-scale shear layers plays an important role in the turbulent kinetic energy dissipation associated with ε_P.

The above results are locally obtained with conditional averages for the shear layers. Their contributions to the global characteristics of turbulence are discussed by comparing the conditional averages with volume averages in the entire computational domain. Figure 21(a) shows the Wi dependence of the mean production and polymer-stress terms of enstrophy in (4.1). The mean values are evaluated with the volume averages, $\langle P_\omega \rangle$ and $\langle V_\omega \rangle$, or the conditional averages at the centre of shear layers, $\overline{P_\omega}$ and $\overline{V_\omega}$. At large Wi, both terms contribute to the enstrophy growth. Therefore, these averages are normalised by the sum of two terms, $\langle P_\omega + V_\omega \rangle$ or $\overline{P_\omega + V_\omega}$. For the shear layer, $\overline{P_\omega}$ and $\overline{V_\omega}$ respectively decrease and increase with Wi, as discused above. The same trend is observed for the volume averages. Figure 21(b) provides a similar comparison for the kinetic energy dissipation rates due to the viscous and polymer stresses. The averages of these dissipation rates normalised by the total dissipation rate are plotted against Wi. For both averages, the viscous dissipation rate decreases with Wi, whereas the dissipation rate due to the polymer stress increases with Wi. The Wi dependence is also similar for both averages. The agreement between these two averages indicates that the Wi dependence of the volume-averaged quantities is well explained by the changes in the shear layers at high Wi, and that the shear layers are important in the global characteristics of viscoelastic turbulence. In figure 21, the error bars illustrate the

range of values obtained from two separate datasets. The narrow range of these error bars suggests that the statistical errors are negligible.

5. Conclusions

Small-scale shear layers arising from turbulent velocity fluctuations are investigated with DNS of statistically stationary homogeneous isotropic turbulence of Newtonian and viscoelastic fluids, where the FENE-P model describes the latter. By identifying the position and orientation of each shear layer with the triple decomposition, the mean flow field around the shear layers is analysed with conditional averages taken in a shear coordinate defined with the shear orientation. The viscoelastic effects are discussed as function of the Weissenberg number Wi, which is the time scale ratio between the maximum relaxation time of the polymer molecules and the Kolmogorov time scale. The present work focuses on the characteristics of local shear layer regions, which play a crucial role in the dissipation mechanisms of turbulent flows. The motivation to study the dissipation mechanism in viscoelastic turbulent flows stems from the well-known depletion of viscous dissipation rates observed in these flows. This phenomenon potentially relates to the dissipation reduction, and thus drag reduction, observed in other types of flows, such as pipe and channel flows of viscoelastic fluids.

The shear layers at high Wi have a large aspect ratio related to small thickness and large length in the layer-parallel direction. The intensities of local fluid motions described by the triple decomposition vary with Wi. As Wi increases, shearing motion becomes more significant while rigid-body rotation and elongation weaken. Rigid-body rotation is manifested as vortex tubes in turbulence. Because of this Wi dependence, the shear layers in viscoelastic turbulence are more dominant as small-scale structures than the vortex tubes. The vortex formation from shear layers, triggered by the shear instability, occurs in both Newtonian and viscoelastic fluids. This instability also results in the fragmentation of shear layers, leading to the formation of smaller structures. However, in the viscoelastic case, this process unfolds more gradually and is observed less frequently. The suppressed instability of shear layers in viscoelastic turbulence explains the prevalence of larger and flatter shear layers, as well as the dominance of shear layers over vortex tubes.

The mean flow field around the shear layers has been examined in a shear coordinate system in figure 6(a). For both Newtonian and viscoelastic turbulence, the shear layers are formed in a straining flow with extensive strain in the vorticity direction of shear and compressive strain in the layer-normal direction. The mean velocity gradient due to shear is independent of Wi when it is normalised by the Kolmogorov scale. However, the extensive strain becomes weak as Wi increases. Similarly, the compressive strain tends to be weak, although this variation is less significant than the observed for the extensive strain. Therefore, the extensive and compressive strains are not balanced at large Wi, unlike in the Newtonian and low Wi cases. This imbalance is significant for sufficiently large Wi, which is $Wi \gtrsim 2$ for the present DNS.

These mean velocity gradients of the shear and biaxial strain affect the polymer-stress distribution near the shear layer. Because the straining flow causes the polymer stretching and compression, the normal polymer stresses in the shear-vorticity direction and the layer-normal direction are locally strengthened and weakened, respectively, within the shear layer. The velocity gradient of the shear causes considerable tangential polymer stress in the shear-flow orientation. Because the strain acting on the shear layer is observed regardless of Wi, the distributions of these stress components are also similar for all Wi. However, the Wi dependence is observed for other components. The imbalance in the straining flow discussed above can cause an additional extensive strain in the layer-parallel direction only for $Wi \gtrsim 2$. In this case, the corresponding polymer stress, the normal stress in the shear-flow direction, becomes large within the shear layer. This component for low Wi has large values outside the

shear layer. Thus, its distribution near the shear layer drastically changes once Wi exceeds about 2.

The enstrophy budget and kinetic energy dissipation were also investigated near the shear layers. The enstrophy production is very active in the shear layer because the extensive strain causes the stretching of vorticity due to shear. The viscous effect transfers enstrophy from the centre of the shear layer to the outside, where the viscous dissipation of enstrophy actively occurs. The polymers also affect the enstrophy budget near the shear layers. First, a thinner shear layer at large Wi causes a greater viscous diffusion because of the large enstrophy gradient. In addition, vortex stretching due to the strain is weakened at high Wi because the extensive strain is weakened. These variations with Wi are associated with the changes in the flow field around the shear layers caused by the viscoelastic effects. The direct interaction between vorticity and polymer stresses also influences the enstrophy evolution. The role of this interaction changes with Wi: it causes the destruction and production of enstrophy within the shear layers at low and high Wi, respectively. The vorticity due to the shear dominates the enstrophy production and destruction due to the polymer stresses in the shear layer. In addition, the normal polymer stress in the shear-flow direction is related to the observed Wi dependence of the vorticity and polymer interaction. This stress component is large within and outside the shear layer at high and low Wi, respectively, and this different distribution causes different roles of the polymer stress in the enstrophy budget. The Wi dependence of the vorticity and polymer interaction is also related to the imbalance between stretching and compression of the straining flow, which is significant only at high Wi. For the kinetic energy dissipation rate within the shear layer, the contribution from the polymer stresses becomes more important as Wi becomes large. This dissipation within the shear layer is also related to the components of the polymer stress tensor enhanced by the shear and strain.

Finally, the Wi dependences of the enstrophy production by vortex stretching, the enstrophy production/destruction due to the polymer and vorticity interaction and the kinetic energy dissipation rates due to viscous and polymer stresses are compared for the averages within the shear layers and the averages in the entire flow region. The Wi dependence of these quantities is similar for both averages, suggesting that the shear layers dominate these phenomena. Crucially, it is suggested that both viscous and polymer kinetic energy dissipations occur predominantly within these shear layers, highlighting the significant role that shear layers play in the dissipation reduction in viscoelastic turbulence.

For Newtonian turbulence, these statistical properties of the shear layers have been compared well with Burgers' vortex layer (Watanabe *et al.* 2020; Hayashi *et al.* 2021*a*). The instability of simple shear flows has also been studied with idealised models (Corcos & Lin 1984; Lin & Corcos 1984; Beronov & Kida 1996). For small-scale shear layers, such models can be developed based on the mean flow field observed around shear layers, as has been successfully reported for Newtonian turbulence (Watanabe & Nagata 2023). These models have demonstrated their capability to reproduce the unstable behavior of shear layers within turbulent flows, including their response to perturbations. This aspect is crucial for flow control strategies that target small-scale turbulent structures (Watanabe 2024) and for understanding the scale-by-scale interaction of turbulent motions (Watanabe & Nagata 2023). Extending these model-based studies to viscoelastic turbulence is feasible based on the present findings, providing an interesting framework to understand viscoelastic turbulence with turbulent structures.

Acknowledgements. We acknowledge PRACE for awarding us access to resource Marenostrum IV based in Spain at https://www.bsc.es. The authors acknowledge Minho Advanced Computing Center for providing HPC computing and consulting resources that have contributed to the research results reported in this paper (https://macc.fccn.pt). This work was also partially supported by the Collaborative Research Project on

Computer Science with High-Performance Computing in Nagoya University and the HPCI System Research Project (hp230045).

Funding. This work was supported by JSPS KAKENHI Grant Numbers JP22K03903 and JP22H01398.

Declaration of interests. The authors report no conflict of interest.

Data availability statement. The data that support the findings of this study are available from the corresponding author upon reasonable request.

REFERENCES

Abreu, H., Pinho, F. T. & da Silva, C. B. 2022 Turbulent entrainment in viscoelastic fluids. *J. Fluid Mech.* **934**, A36.

Adrian, R. J., Meinhart, C. D. & Tomkins, C. D. 2000 Vortex organization in the outer region of the turbulent boundary layer. *J. Fluid Mech.* **422**, 1–54.

Alvelius, K. 1999 Random forcing of three-dimensional homogeneous turbulence. *Phys. Fluids* **11** (7), 1880–1889.

Beronov, K. N. & Kida, S. 1996 Linear two-dimensional stability of a Burgers vortex layer. *Phys. Fluids* **8** (4), 1024–1035.

Bhatt, K. & Tsuji, Y. 2021 Identification of vortex structures in flow fields using tomographic PIV method. *J. Fluid Sci. Tech.* **16** (3), JFST0018–JFST0018.

Bird, R. B., Curtiss, C. F., Armstrong, R. C. & Hassager, O. 1987 *Dynamics of polymeric liquids, volume 2: Kinetic theory*. Wiley.

Bird, R. B., Dotson, P. J. & Johnson, N. L. 1980 Polymer solution rheology based on a finitely extensible bead-spring chain model. *J. Non-Newtonian Fluid Mech.* **7**, 213–235.

Buxton, O. R. H. & Ganapathisubramani, B. 2010 Amplification of enstrophy in the far field of an axisymmetric turbulent jet. *J. Fluid Mech.* **651**, 483–502.

Cai, W.-H., Li, F.-C. & Zhang, H.-N. 2010 DNS study of decaying homogeneous isotropic turbulence with polymer additives. *J. Fluid Mech.* **665**, 334–356.

Chen, X., Chung, Y. M. & Wan, M. 2021 The uniform-momentum zones and internal shear layers in turbulent pipe flows at Reynolds numbers up to $re_\tau = 1000$. *Int. J. Heat Fluid Flow* **90**, 108817.

Chong, M. S., Perry, A. E. & Cantwell, B. J. 1990 A general classification of three-dimensional flow fields. *Phys. Fluids* **2** (5), 765–777.

Corcos, G. M. & Lin, S. J. 1984 The mixing layer: deterministic models of a turbulent flow. Part 2. The origin of the three-dimensional motion. *J. Fluid Mech.* **139**, 67–95.

Corrsin, S. & Kistler, A. L. 1955 Free-stream boundaries of turbulent flows. *NACA Technical Report No. TN-1244* .

Das, R. & Girimaji, S. S. 2020 Revisiting turbulence small-scale behavior using velocity gradient triple decomposition. *New J. Phys.* **22** (6), 063015.

Davidson, P. A. 2004 *Turbulence: An Introduction for Scientists and Engineers*. Oxford Univ. Pr.

De Angelis, E., Casciola, C. M., Benzi, R. & Piva, R. 2005 Homogeneous isotropic turbulence in dilute polymers. *J. Fluid Mech.* **531**, 1–10.

Eisma, J., Westerweel, J., Ooms, G. & Elsinga, G. E. 2015 Interfaces and internal layers in a turbulent boundary layer. *Phys. Fluids* **27** (5), 055103.

Elsinga, G. E., Ishihara, T., Goudar, M. V., da Silva, C. B. & Hunt, J. C. R. 2017 The scaling of straining motions in homogeneous isotropic turbulence. *J. Fluid Mech.* **829**, 31–64.

Elsinga, G. E. & Marusic, I. 2010 Universal aspects of small-scale motions in turbulence. *J. Fluid Mech.* **662**, 514–539.

Elsinga, G. E. & Marusic, I. 2016 The anisotropic structure of turbulence and its energy spectrum. *Phys. Fluids* **28** (1), 011701.

Enoki, R., Watanabe, T. & Nagata, K. 2023 Statistical properties of shear and nonshear velocity components in isotropic turbulence and turbulent jets. *Phys. Rev. Fluids* **8** (10), 104602.

Fan, D., Xu, J., Yao, M. X. & Hickey, J.-P. 2019 On the detection of internal interfacial layers in turbulent flows. *J. Fluid Mech.* **872**, 198–217.

Ferreira, P. O., Pinho, F. T. & da Silva, C. B. 2016 Large-eddy simulations of forced isotropic turbulence with viscoelastic fluids described by the FENE-P model. *Phys. Fluids* **28** (12), 125104.

968 Fiscaletti, D., Buxton, O. R. H. & Attili, A. 2021 Internal layers in turbulent free-shear flows. *Phys. Rev.*
969 *Fluids* **6** (3), 034612.
970 Ganapathisubramani, B., Lakshminarasimhan, K. & Clemens, N. T. 2008 Investigation of three-
971 dimensional structure of fine scales in a turbulent jet by using cinematographic stereoscopic particle
972 image velocimetry. *J. Fluid Mech.* **598**, 141–175.
973 Ghira, A. A., Elsinga, G. E. & da Silva, C. B. 2022 Characteristics of the intense vorticity structures in
974 isotropic turbulence at high Reynolds numbers. *Phys. Rev. Fluids* **7** (10), 104605.
975 Goudar, M. V. & Elsinga, G. E. 2018 Tracer particle dispersion around elementary flow patterns. *J. Fluid*
976 *Mech.* **843**, 872–897.
977 Graham, M. D. 2014 Drag reduction and the dynamics of turbulence in simple and complex fluids. *Phys.*
978 *Fluids* **26** (10), 101301.
979 Green, M. A., Rowley, C. W. & Haller, G. 2007 Detection of lagrangian coherent structures in three-
980 dimensional turbulence. *J. Fluid Mech.* **572**, 111–120.
981 Guimarães, M. C., Pimentel, N., Pinho, F. T. & da Silva, C. B. 2020 Direct numerical simulations of
982 turbulent viscoelastic jets. *J. Fluid Mech.* **899**, 11–37.
983 Guimarães, M. C., Pinho, F. T. & da Silva, C. B. 2022 Turbulent planar wakes of viscoelastic fluids
984 analysed by direct numerical simulations **946**, A26.
985 Guimarães, M. C., Pinho, F. T. & da Silva, C. B. 2023 Viscoelastic jet instabilities studied by direct
986 numerical simulations. *Phys. Rev. Fluids* **8** (10), 103301.
987 Gul, M., Elsinga, G. E. & Westerweel, J. 2020 Internal shear layers and edges of uniform momentum
988 zones in a turbulent pipe flow. *J. Fluid Mech.* **901**, A10.
989 Haller, G.eorge 2023 *Transport Barriers and Coherent Structures in Flow Data*. Cambridge University
990 Press.
991 Haller, G., Hadjighasem, A., Farazmand, M. & Huhn, F. 2016 Defining coherent vortices objectively
992 from the vorticity. *J. Fluid Mech.* **795**, 136–173.
993 Hayashi, M., Watanabe, T. & Nagata, K. 2021*a* Characteristics of small-scale shear layers in a temporally
994 evolving turbulent planar jet. *J. Fluid Mech.* **920**, A38.
995 Hayashi, M., Watanabe, T. & Nagata, K. 2021*b* The relation between shearing motions and the
996 turbulent/non-turbulent interface in a turbulent planar jet. *Phys. Fluids* **33** (5), 055126.
997 Horiuti, K. & Fujisawa, T. 2008 The multi-mode stretched spiral vortex in homogeneous isotropic
998 turbulence. *J. Fluid Mech.* **595**, 341–366.
999 Horiuti, K., Matsumoto, K. & Fujiwara, K. 2013 Remarkable drag reduction in non-affine viscoelastic
1000 turbulent flows. *Phys. Fluids* **25** (1).
1001 Horiuti, K. & Takagi, Y. 2005 Identification method for vortex sheet structures in turbulent flows. *Phys.*
1002 *Fluids* **17** (12), 121703.
1003 Jahanbakhshi, R., Vaghefi, N. S. & Madnia, C. K. 2015 Baroclinic vorticity generation near the
1004 turbulent/non-turbulent interface in a compressible shear layer. *Phys. Fluids* **27** (10), 105105.
1005 Jeong, J. & Hussain, F. 1995 On the identification of a vortex. *J. Fluid Mech.* **285**, 69–94.
1006 Jiang, X., Lefauve, A., Dalziel, S. B. & Linden, P. F. 2022 The evolution of coherent vortical structures
1007 in increasingly turbulent stratified shear layers. *J. Fluid Mech.* **947**, A30.
1008 Jiménez, J. & Wray, A. A. 1998 On the characteristics of vortex filaments in isotropic turbulence. *J. Fluid*
1009 *Mech.* **373**, 255–285.
1010 Jiménez, J., Wray, A. A., Saffman, P. G. & Rogallo, R. S. 1993 The structure of intense vorticity in
1011 isotropic turbulence. *J. Fluid Mech.* **255**, 65–90.
1012 Kalelkar, C., Govindarajan, R. & Pandit, R. 2005 Drag reduction by polymer additives in decaying
1013 turbulence. *Phys. Rev. E* **72** (1), 017301.
1014 Kang, H. S. & Meneveau, C. 2008 Experimental study of an active grid-generated shearless mixing layer
1015 and comparisons with large-eddy simulation. *Phys. Fluids* **20** (12), 125102.
1016 Keylock, C. J. 2018 The Schur decomposition of the velocity gradient tensor for turbulent flows. *J. Fluid*
1017 *Mech.* **848**, 876–905.
1018 Kim, K., Li, C.-F., Sureshkumar, R., Balachandar, S. & Adrian, R. J. 2007 Effects of polymer stresses
1019 on eddy structures in drag-reduced turbulent channel flow. *J. Fluid Mech.* **584**, 281–299.
1020 Kolář, V. 2007 Vortex identification: New requirements and limitations. *Int. J. Heat Fluid Flow* **28** (4),
1021 638–652.
1022 Kolář, V. & Šístek, J. 2014 Recent progress in explicit shear-eliminating vortex identification. In
1023 *Proceedings of the 19th Australasian Fluid Mechanics Conference*.

Kronborg, J. & Hoffman, J. 2023 The triple decomposition of the velocity gradient tensor as a standardized real Schur form. *Phys. Fluids* **35** (3), 031703.

Li, W. & Graham, M. D. 2007 Polymer induced drag reduction in exact coherent structures of plane poiseuille flow. *Phys. Fluids* **19**, 083101.

Lin, S. J. & Corcos, G. M. 1984 The mixing layer: deterministic models of a turbulent flow. Part 3. The effect of plane strain on the dynamics of streamwise vortices. *J. Fluid Mech.* **141**, 139–178.

Liu, C., Gao, Y., Tian, S. & Dong, X. 2018 Rortex-A new vortex vector definition and vorticity tensor and vector decompositions. *Phys. Fluids* **30** (3), 035103.

Maciel, Y., Robitaille, M. & Rahgozar, S. 2012 A method for characterizing cross-sections of vortices in turbulent flows. *Int. J. Heat Fluid Flow* **37**, 177–188.

Nagata, R., Watanabe, T., Nagata, K. & da Silva, C. B. 2020 Triple decomposition of velocity gradient tensor in homogeneous isotropic turbulence. *Comput. Fluids* **198**, 104389.

Neamtu-Halic, M. M., Krug, D., Haller, G. & Holzner, M. 2019 Lagrangian coherent structures and entrainment near the turbulent/non-turbulent interface of a gravity current. *J. Fluid Mech.* **877**, 824–843.

Ouellette, N. T., Xu, H. & Bodenschatz, E. 2009 Bulk turbulence in dilute polymer solutions. *J. Fluid Mech.* **629**, 375–385.

Perlekar, P., Mitra, D. & Pandit, R. 2006 Manifestations of drag reduction by polymer additives in decaying, homogeneous, isotropic turbulence. *Phys. Rev. Lett.* **97** (26), 264501.

Pirozzoli, S., Bernardini, M. & Grasso, F. 2010 On the dynamical relevance of coherent vortical structures in turbulent boundary layers. *J. Fluid Mech.* **648**, 325–349.

Sakurai, Y. & Ishihara, T. 2018 Relationships between small-scale fluid motions and inertial particle clustering in turbulence. *J. Phys. Soc. Japan* **87** (9), 093401.

Siggia, E. D. 1981 Numerical study of small-scale intermittency in three-dimensional turbulence. *J. Fluid Mech.* **107**, 375–406.

da Silva, C. B., Dos Reis, R. J. N. & Pereira, J. C. F. 2011 The intense vorticity structures near the turbulent/non-turbulent interface in a jet. *J. Fluid Mech.* **685**, 165–190.

Silva, T. S., Zecchetto, M. & da Silva, C. B. 2018 The scaling of the turbulent/non-turbulent interface at high Reynolds numbers. *J. Fluid Mech.* **843**, 156–179.

Šístek, J., Kolář, V., Cirak, F. & Moses, P. 2012 Fluid-structure interaction and vortex identification. In *Proceedings of the 18th Australasian Fluid Mechanics Conference*. Australasian Fluid Mechanics Society Australia.

Song, J., Lin, F., Liu, N., Lu, X.-Y. & Khomami, B. 2021 Direct numerical simulation of inertio-elastic turbulent Taylor–Couette flow. *J. Fluid Mech.* **926**, A37.

Tanahashi, M., Iwase, S. & Miyauchi, T. 2001 Appearance and alignment with strain rate of coherent fine scale eddies in turbulent mixing layer. *J. Turbulence* **2** (6), 1–18.

Toms, B. A. 1948 Some observations on the flow of linear polymer solutions through straight tubes at large reynolds numbers. In *Proc. Int. Congress of Rheology, Holland, North-Holland, Amsterdam*, , vol. Section II, pp. 135–141.

Tsinober, A. 2009 *An informal conceptual introduction to turbulence*. Springer.

Vaithianathan, T., Robert, A., Brasseur, J. G. & Collins, L. R. 2006 An improved algorithm for simulating three-dimensional, viscoelastic turbulence. *J. Non-Newt. Fluid Mech.* **140** (1), 3–22.

Valente, P. C., da C. B. da Silva & Pinho, F. T. 2014*a* The effect of viscoelasticity on the turbulent kinetic energy cascade. *J. Fluid. Mech.* **760**, 39–62.

Valente, P. C., da C. B. da Silva & Pinho, F. T. 2016 Energy spectra in elasto-inertial turbulence. *Phys. Fluids* **28**, 075108.

Valente, P. C., da Silva, C. B. & Pinho, F. T. 2014*b* The effect of viscoelasticity on the turbulent kinetic energy cascade. *J. Fluid Mech.* **760**, 39–62.

Vincent, A. & Meneguzzi, M. 1991 The satial structure and statistical properties of homogeneous turbulence. *J. Fluid Mech.* **225**, 1–20.

Vincent, A. & Meneguzzi, M. 1994 The dynamics of vorticity tubes in homogeneous turbulence. *J. Fluid Mech.* **258**, 245–254.

Vonlanthen, R. & Monkewitz, P. A. 2013 Grid turbulence in dilute polymer solutions: PEO in water. *J. Fluid Mech.* **730**, 76–98.

Wang, Y., Gao, Y. & Liu, C. 2018 Galilean invariance of Rortex. *Phys. Fluids* **30** (11).

Watanabe, T. 2024 Efficient enhancement of turbulent entrainment by small-scale shear instability. *J. Fluid Mech.* **988**, A20.

Watanabe, T. & Gotoh, T. 2014 Power-law spectra formed by stretching polymers in decaying isotropic turbulence. *Phys. Fluids* **26** (3), 035110.

Watanabe, T., Mori, T., Ishizawa, K. & Nagata, K. 2024 Scale dependence of local shearing motion in decaying turbulence generated by multiple-jet interaction. *J. Fluid Mech.* **997**, A14.

Watanabe, T. & Nagata, K. 2022 Energetics and vortex structures near small-scale shear layers in turbulence. *Phys. Fluids* **34** (9), 095114.

Watanabe, T. & Nagata, K. 2023 The response of small-scale shear layers to perturbations in turbulence. *J. Fluid Mech.* **963**, A31.

Watanabe, T., da Silva, C. B., Nagata, K. & Sakai, Y. 2017 Geometrical aspects of turbulent/non-turbulent interfaces with and without mean shear. *Phys. Fluids* **29** (8), 085105.

Watanabe, T., Tanaka, K. & Nagata, K. 2020 Characteristics of shearing motions in incompressible isotropic turbulence. *Phys. Rev. Fluids* **5** (7), 072601.

White, C. M. & Mungal, M. G. 2008 Mechanics and prediction of turbulent drag reduction with polymer additives. *Annu. Rev. Fluid Mech.* **40** (1), 235–256.

Yamani, S., Raj, Y., Zaki, T. A., McKinley, G. H. & Bischofberger, I. 2023 Spatiotemporal signatures of elastoinertial turbulence in viscoelastic planar jets. *Phys. Rev. Fluids* **8** (6), 064610.